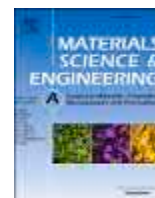Contents lists available at ScienceDirect

Materials Science & Engineering A

Comparative study of hydrogen embrittlement resistance between additively and conventionally manufactured 304L austenitic stainless steels

Dong-Hyun Lee [a,b,*], Binhan Sun [b], Subin Lee [b], Dirk Ponge [b], Eric A. Jägle [b,c], Dierk Raabe [b]

[a] Department of Materials Science and Engineering, Chungnam National University, 34134, Daejeon, Republic of Korea
[b] Department for Microstructure Physics and Alloy Design, Max-Planck-Institut für Eisenforschung GmbH, 40237, Düsseldorf, Germany
[c] Institute of Materials Science, Universität der Bundeswehr München, 85579, Neubiberg, Germany

ARTICLE INFO

ABSTRACT

Hydrogen embrittlement in 304L austenitic stainless steel fabricated by laser powder-bed-fusion (LPBF) was investigated and compared to conventionally produced 304L samples with two different processing histories; casting plus annealing (CA) and CA plus thermomechanical treatment (CA-TMT). Interestingly, no significant difference in the amount of deformation-induced α′ martensite between the LPBF and CA-TMT samples was observed, suggesting that the solidification substructure in the LPBF sample enhanced the strength without promoting the harmful hydrogen embrittlement effect. These results are discussed in terms of the chemical inhomogeneity, hydrogen-assisted cracking behavior, and hydrogen diffusion and trapping in the present 304L samples.

1. Introduction

Austenitic stainless steels (ASSs) are frequently used for sensitive hydrogen (H) storage, hydrogen infrastructure, as well transportation applications, since they are generally less susceptible to hydrogen embrittlement (HE) compared to ferritic steels. This is due to their lower diffusivity and higher solubility of H [1–3]. HE describes a phenomenon in which materials undergo an often abrupt and catastrophic deterioration of their mechanical properties (especially when exposed to tensile loads, due to loss of their tensile ductility) caused by the presence of environmental H in acidic solutions and H-containing gases [4–8] which diffuses into the bulk material. In contrast to thermodynamically stable ASSs (e.g., AISI type 310S) which is less prone to undergo HE, severe HE has often been observed in metastable ASSs containing only 8–10 wt% Ni (e.g., AISI type 304), in which strain-induced α′ martensite forms during deformation [9–11]. The strain-induced α′ martensite offers a fast diffusion path for H, leading to enrichment of H at critical sites in the microstructure (such as micromechanically highly stressed regions in front of hetero-interfaces) and thus H-assisted cracking [12,13]. In addition, a small amount of δ ferrite can be present in metastable ASSs due to segregation during solidification or incomplete δ to γ transformation due to high cooling rates. This may increase the HE susceptibility of the samples by providing crack initiation sites [14,15]. There

are, however, different reports about the HE susceptibility of metastable ASSs in the literature as summarized in Table 1 [10,13,16–19]. For example, Egels et al. [18] showed that 304 ASSs having very similar nominal compositions can exhibit very different HE susceptibilities due to segregation effects resulting from different production routes. In regions where segregation increases austenite stability, the martensitic transformation was suppressed, which caused a slow H uptake/diffusion rate and thus slow crack growth rate. It has been reported that pre-deformation in 304 ASS leads to the martensitic transformation and thus affects its HE susceptibility [13,16,20]. These studies clarify the impact of metallurgical aspects such as grain size, local segregation (caused by different production routes), and volume fraction of α′ martensite on the HE susceptibility of 304 ASS. Note that some researchers have also found the formation of ε martensite as a precursor for α′ martensite [21–24], however this mechanism has not been reported in the literature on HE of metastable ASSs [10,13,16–19]. We will discuss the possibility of forming ε martensite in the following section.

Recently, additive manufacturing processes such as directed energy deposition and laser powder-bed-fusion (LPBF), have emerged as a promising manufacturing technology, in which three-dimensional parts are printed by progressively adding thin layers of powder material and consolidating them by melting with a laser beam [25–27]. It has become possible for a number of metals (including steels, aluminum alloys, and

titanium alloys) to reliably manufacture highly complex or customized parts directly from a computer-coded design file and raw material powder [25–30]. Additive manufacturing processes have thus the potential to replace many conventional production processes.

LPBF-processed ASSs often exhibit highly complex and hierarchical microstructures (e.g., irregular grain structure and solidification substructure) accompanied by elemental segregation due to the combination of high cooling rate ($\sim10^5$-10^6 K/s) and high thermal stress [31–33], which are not accessible through conventional manufacturing routes, such as casting or forging. In this regard, the LPBF process significantly alters the metallurgical aspects described in Table 1 and thus the H effects in LPBF-processed metastable ASSs can be expected to be very different from those in their conventional counterparts. Accordingly, the analysis of the H effects in LPBF-processed metastable ASSs is essential for examining the possibility of the future use of LPBF-manufactured parts in infrastructures with strong H exposure. Until now, very little research on the issue is available in the literature [34]. The only available study in this field [34] reported that directed energy deposition-processed 304L was less susceptible to HE than wrought 304L, and attributed the high HE resistance in additively manufactured 304L to its high austenite stability. However, this previous study did not reveal which specific additive manufacturing-induced microstructural change was responsible for the difference in HE resistance, i.e. austenite stability (due to chemical inhomogeneity), the characteristic cellular solidification microstructure or other features. Accordingly, in the present study, we aim to close this gap. We examine here if the trend that additively manufactured 304L shows high HE resistance is reproducible also for the LPBF process and we provide a more detailed and systematic investigation into the underlying mechanisms of H-assisted failure in additively manufactured 304L. We do this by comparing LPBF-produced material to conventionally-produced 304L ASSs subjected to two different processing histories. The first conventionally-produced reference material has been cast and annealed and the second conventionally-produced reference sample has been cast and annealed, followed by an additional thermomechanical treatment. As shown below, this allows us to systematically separate effects associated with the influence of austenite stability, chemical inhomogeneity, and cellular microstructure. We systematically investigate HE in LPBF- and conventionally processed 304L ASS through tensile testing with and without electrochemical H pre-charging.

2. Materials and experiments

Gas-atomized spherical 304L ASS powder (~45 μm D50, provided by LPW Technologies) with the nominal composition listed in Table 2 was used in this study. A block of 304L ASS with the size of 20 mm (width) × 60 mm (length) × 30 mm (thickness) was fabricated by LPBF (Aconity Mini, Aconity 3D GmbH, Aachen, Germany). During the LPBF process, the layer thickness, laser power and scan speed were set as 30 μm, 180 W, and 700 mm/s, respectively. The laser scanned line by line along the same direction in each layer with a hatch spacing of 80 μm, and the scanning direction was rotated by 90° after each layer. The as-built sample is referred to as the LPBF sample.

The 304L ASS specimen produced by strand casting and subsequent solution annealing at 1050 °C for 30 min (hereafter designated as the CA sample) was supplied from SeAH Steel and cut into a disk with a size of 60 mm (diameter) × 50 mm (thickness). To clarify the effect of thermomechanical treatment (TMT) on HE in the CA sample, a part of the material was, after casting and annealing, subjected to hot-rolling at 1000 °C to a thickness reduction of 50% and subsequently homogenized at 1150 °C for 18 h in Ar atmosphere. Finally, the sample was cold-rolled to a thickness reduction of ~70% and annealed at 1050 °C for 1 h, followed by water quenching. The CA sample subjected to TMT will be referred to as the CA-TMT sample. Thus, there are three different

Table 1

Comparison of metallurgical aspects, H-charging conditions, and resultant HE index in various 304 ASSs from literature. HE index represents the ratio of the elongation (or reduction of area) of the H charged sample, $\varepsilon_{f,H}$, to that of the uncharged sample, $\varepsilon_{f,0}$, which are measured from tensile tests at room temperature. Note that HE susceptibility increases with decreasing HE index ($\varepsilon_{f,H}/\varepsilon_{f,0}$). H charging was conducted either before tensile test or during the test, which are represented as Pre- and In-situ, respectively. H content was measured by thermal desorption spectrometry; the values marked with * mean H content exclusively at brittle H affected zone. Detailed information can be found in each reference.

Metallurgical aspect	H charging condition						H content [wt. ppm]	HE index	Ref.
Heat treatment	Charging method	H_2 pressure [MPa]	Current density [mA/cm^2]	Time [h]	Temp. [°C]				
Solution annealed	Gaseous H charging	1	–	Duration of tensile test (In-situ)	RT		–	~0.53	[9]
Sensitized								~0.29	
Sensitized + desensitized								~0.51	
Production route									
Casting	Gaseous H charging	40	–	Duration of tensile test (In-situ)	RT		–	~0.50	[18]
Electroslag remelting								~0.89	
Grain size [μm]									
12	Electro-chemical H charging	–	10	Duration of tensile test (In-situ)	RT		–	~0.80	[19]
8								~0.84	
4								~0.95	
Single crystal	Electro-chemical H charging	–	2.7	7 (Pre-)	80		–	~0.43	[17]
0.46							124	~0.67	
0.32							126	~0.86	
0.14							170	~0.84	
0.09							–	~0.80	
Pre-strain % (prior α′ vol%)									
0 (0)	Gaseous H charging	30	–	48 (Pre-)	200		~48	~0.67	[13]
12 (31)							~39	~0.79	
20 (60)							~22	~0.92	
30 (96)							~6	~0.99	
0 (0)	Electro-chemical H charging	–	50	96 (Pre-)	RT		~606.5*	~0.93	[16]
3 (1)							–	~0.93	
6 (3)							–	~0.91	
10 (8)							~834.8*	~0.82	
15 (20)							–	~0.71	
20 (37)							~580.7*	~0.65	
25 (57)							–	~0.30	

Table 2
Chemical compositions (wt.%) of 304L ASSs investigated in this study.

Material	C	Cr	Cu	Mn	N	Ni	O	P	S	Si	Fe
Powder	0.017	18.4	<0.1	1.3	0.060	9.90	0.03	0.018	0.004	0.63	Bal.
LPBF	0.017	18.3	0.029	1.2	0.055	9.94	0.03	0.002	0.007	0.63	Bal.
CA(-TMT)	0.025	18.2	0.453	1.87	0.075	9.01	–	0.031	0.018	0.34	Bal.

samples that were tested here; samples LPBF, CA, and CA-TMT. The compositions of these samples were analyzed by inductively coupled plasma optical emission spectrometry and the results are also listed in Table 2. Due to the different production routes, the LPBF and the CA (-TMT) samples vary slightly in chemical composition.

To estimate the different austenite stability of all samples due to these slight compositional differences, the thermodynamic driving force for α' martensite transformation was estimated by calculating $\Delta G^{\gamma \to \alpha}$ ($=G_\alpha - G_\gamma$, where G_γ and G_α are Gibbs free energies of γ austenite and α ferrite, respectively) using the Thermo-Calc software, version 2018a, in conjunction with the TCFE9 database. The calculations were carried out for a temperature of 298 K considering the chemical compositions shown in Table 2. The values of $\Delta G^{\gamma \to \alpha}$ for samples LPBF and CA(-TMT) are calculated as −2.66 kJ/mol and −2.57 kJ/mol, respectively, i.e. the austenite in the CA(-TMT) sample is only very slightly more stable than that in the LPBF sample. In addition, the driving force for ε martensite transformation, $\Delta G^{\gamma \to \varepsilon}$ ($=G_\varepsilon - G_\gamma$, where G_ε is Gibbs free energy of ε), was also calculated. $\Delta G^{\gamma \to \varepsilon}$ values (−0.50 kJ/mol and −0.61 kJ/mol for samples LPBF and CA(-TMT), respectively) are much lower than $\Delta G^{\gamma \to \alpha}$ values, indicating that α' martensite transformation is thermodynamically more favorable in the present 304L ASSs. As a second approach to estimate the austenite stability, the M_{d30} temperature, which represents the temperature at which 50 vol.% of the austenite transforms to martensite with an applied true strain of 30%, is calculated by using the following empirical expression [35,36]:

$$M_{d30}(^\circ C) = 551 - 462(C + N) - 9.2Si - 8.1Mn - 13.7Cr - 29Ni - 18.5Mo - 29Cu - 68Nb - 1.42(\text{grain size number (ASTM)} - 8)$$

(1)

where all elements are counted in weight percentage (wt. %). The M_{d30} temperature serves as an approximate parameter representing the mechanical stability of the austenite against deformation-inducted martensite formation; a lower M_{d30} temperature means a higher mechanical stability of austenite. Based on the chemical composition in Table 2 and Eq. (1), M_{d30} of the LPBF and CA(-TMT) samples were

calculated to be ∼ −34.7 °C and ∼−34.4 °C, respectively. Considering these insignificant differences in $\Delta G^{\gamma \to \alpha}$ and M_{d30} between samples LPBF and CA(-TMT), the austenite stability of LPBF can be considered as very similar to that of CA(-TMT), which suggests that the CA(-TMT) sample can serve as a reference material in this study.

Flat, dog-bone-shaped tensile samples with gauge dimensions of 2 mm (width) × 4 mm (length) × 1 mm (thickness) were machined by spark erosion from the LPBF-produced block and ground mechanically. For all the samples, tensile specimens were cut along the Y direction in the horizontal plane (XY plane) as shown in Fig. 1. Note that the Z direction is parallel to the building direction for the LPBF sample, whereas the Y direction is parallel to the rolling direction for the CA-TMT sample. Tensile specimens were mechanically ground with fine SiC paper (grit number up to 2000).

In order to introduce H into the specimen, electrochemical H-charging was carried out at room temperature with a potentiostat using a 2 g/l CH_4N_2S (hydrogen recombination agent) in 0.5 M H_2SO_4 solution (pH = 1). H-charging was performed under two different conditions; one set of samples was H pre-charged for 1 day at a constant current density of 20 mA/cm^2, and another set was H pre-charged at 50 mA/cm^2 for 5 days. Increased current density and charging time was adopted for the second set in order to more effectively enhance the H adsorption. To minimize the influence of outgassing, all further experiments on H pre-charged samples were started within 30 min after H-charging. Tensile tests were performed on both uncharged and H pre-charged samples using a tensile stage (Kammrath & Weiss, Dortmund, Germany) at a cross-head speed of 0.4 μm/s, which corresponds to an initial strain rate of 10^{-4}/s. The digital image correlation technique was carried out to determine the local plastic strain during tensile deformation and the obtained data was analyzed using Aramis software (GOM GmbH, Braunschweig, Germany). At least three tests were conducted for each condition to confirm reproducibility.

The microstructure of the specimens was characterized by an EBSD detector (Digiview, EDAX-TSL, Mahwah, NJ) mounted on a scanning electron microscope (SEM; JSM 6500F, JEOL Ltd., Tokyo, Japan),
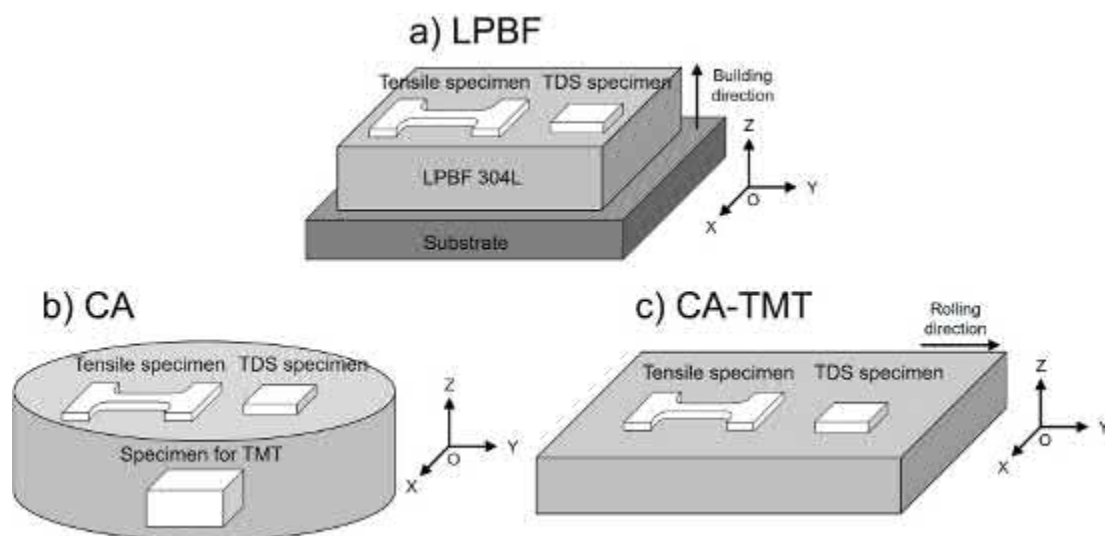
Fig. 1. Schematic illustrations of the (a) LPBF, (b) CA, and (c) CA-TMT samples, as cut for tensile testing and TDS measurements. (LPBF: Laser powder-bed-fusion, TDS: Thermal desorption spectroscopy).

electron channeling contrast imaging (ECCI; Merlin, Carl Zeiss AG, Oberkochen, Germany), and transmission electron microscopy (TEM; JEM 2200FS, JEOL Ltd., Tokyo, Japan) in scanning TEM (STEM) mode. The EBSD analysis was conducted at 15 kV acceleration voltage with a beam step size of 50 nm–1 μm. For SEM probing, the samples were mechanically ground and subsequently polished with 3 μm diamond suspension and finally with 0.05 μm silica suspension. TEM specimens were prepared by focused ion beam milling with a Nova 600 NanoLab (FEI Co., Hillsboro, OR). During SEM and TEM analysis, element mapping was performed using energy dispersive X-ray spectroscopy (EDS).

The H desorption behavior was analyzed by using a custom-designed ultra-high vacuum based thermal desorption spectroscope (TDS) equipped with a mass spectrometer detector. During the TDS measurements, the samples were heated up to 800 °C at a constant heating rate of 26 K/min. The total H content was determined by measuring the cumulative amount of the desorbed H from room temperature up to 800 °C. Note that the specimens subjected to TDS probing were also cut from the horizontal plane (see Fig. 1).

3. Results

3.1. Initial microstructure and the effects of H on the tensile properties

The microstructural characterization of the LPBF sample by EBSD and ECCI is shown in Fig. 2. The inverse pole figure map of the LPBF sample (Fig. 2a) reveals that the grains of the sample exhibit a highly irregular shape with a wide range of sizes (~1–80 μm) which is attributed to the track-wise melting of material and the high temperature gradient during the solidification. The average grain size is estimated to be ~47 μm measured by counting only high-angle grain boundaries (>15°). The LPBF sample consists of a single-phase austenite structure with a large fraction of low-angle grain boundaries (2–15°), ~60% of the total GBs (see Fig. 2b). As shown in Fig. 2c, there is some degree of texture with respect to building direction. However, no strong texture is developed along the direction perpendicular to the building direction. Furthermore, Fig. 2d displays an ECCI image of the LPBF sample,

revealing that a solidification cellular structure is formed inside the individual grains. The average size of this cellular structure is ~350 nm in diameter (which is substantially smaller than that of the grains) and a large number of dislocations are concentrated at the walls of the cells (Fig. 2e), similar to the cell structures reported in Al-, Co-, and Fe-based samples fabricated by the LPBF process [31,32,37]. When solidification cells grow together into coarse single grains under a high temperature gradient and at high growth rate conditions, the slight orientation difference between neighboring cells causes the high density of such dislocation walls [32,38].

In contrast to the LPBF sample, the inverse pole figure map of the CA sample (Fig. 3a) shows regular polygonal grains with a large fraction of annealing twins. The estimated average grain size of the CA sample is ~51 μm (including twin boundaries). More importantly, retained δ ferrite is present in the γ austenite matrix (Fig. 3b), which is not observed in the LPBF sample, and its volume fraction is ~1 vol.%. This implies that the solution annealing at 1050 °C for 30 min is insufficient to remove δ formed during casting. Fig. 3d and 3e display the inverse pole figure map and the corresponding phase map for the same area of the CA-TMT sample, respectively. It is evident that the CA-TMT sample has a slightly larger grain size (~62 μm) than the CA sample (Fig. 3d) and, more importantly, TMT completely eliminates the retained δ ferrite (Fig. 3e). These results clearly suggest that the 304L sample produced by strand casting requires an additional TMT for achieving a fully austenitic structure, in contrast to the 304L sample produced by LPBF. As noted in Fig. 3c and 3f, no strong crystallographic texture has developed with respect to the Y direction (or rolling direction) in the CA and CA-TMT samples. For all the samples, the IPFs and the corresponding IPF maps with respect to the X, Y, and Z directions are provided in the Supplementary Material section.

In summary, the results presented in Figs. 2 and 3 demonstrate that large temperature gradients and rapid solidification as imposed during the LPBF process imparts three crucial changes to the microstructure in 304L ASS compared to conventional materials (especially compared to the CA sample): (i) fully austenitic structure without any further processing step, (ii) irregular shaped grains with a wide range of sizes, and
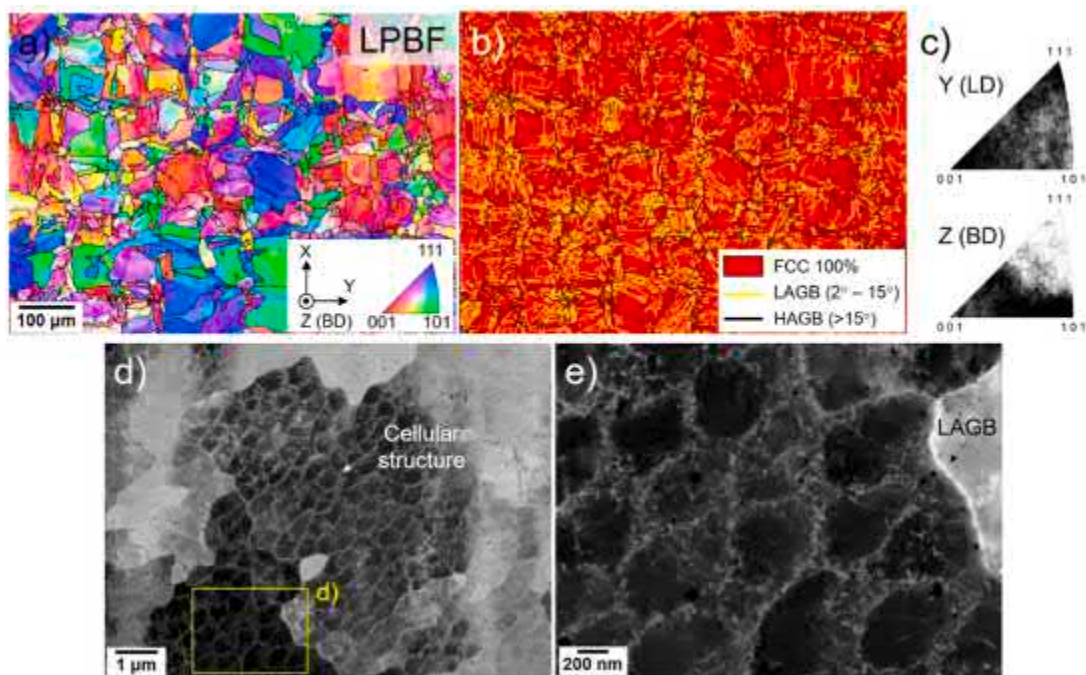

Fig. 2. Microstructure of the LPBF sample: (a) EBSD inverse pole figure map with respect to the Y direction, (b) EBSD phase map with grain boundaries superimposed, (c) inverse pole figures (EBSD step size: 1 μm), (d) ECCI image showing a cellular substructure, and (e) magnified ECCI image of a selected area in (d). The information on X, Y, and Z directions are provided in Fig. 1. (LPBF: Laser powder-bed-fusion, BD: Building direction, LD: Loading direction).
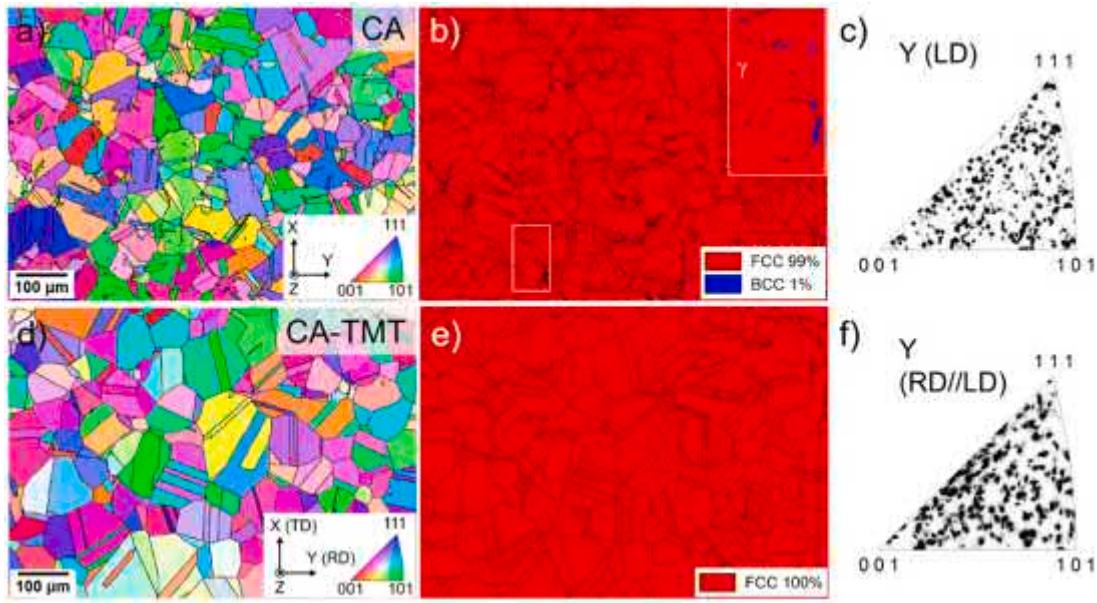
Fig. 3. Microstructure of samples (a,b,c) CA and (d,e,f) CA-TMT: (a) and (d) EBSD inverse pole figure map with respect to Y direction; (b) and (e) EBSD phase map; (c) and (f) inverse pole figure. The information on X, Y, and Z directions are provided in Fig. 1. (EBSD step size: 1 μm, CA: Casting plus annealing, TMT: Thermomechanical treatment, RD: Rolling direction, TD: Transverse direction, LD: Loading direction).

(iii) the presence of a large fraction of low-angle grain boundaries and the associated cellular substructure within the individual grains.

Representative engineering stress vs. engineering strain responses of the LPBF, CA, and CA-TMT samples, as well as those of their H-charged counterparts (charged for 1 and 5 days) are shown in Fig. 4. Prior to H-charging, the LPBF sample exhibits a higher yield strength (~520 MPa) compared to the CA and CA-TMT samples (~340 MPa and ~240 MPa, respectively), due to the high density of low-angle grain boundaries and
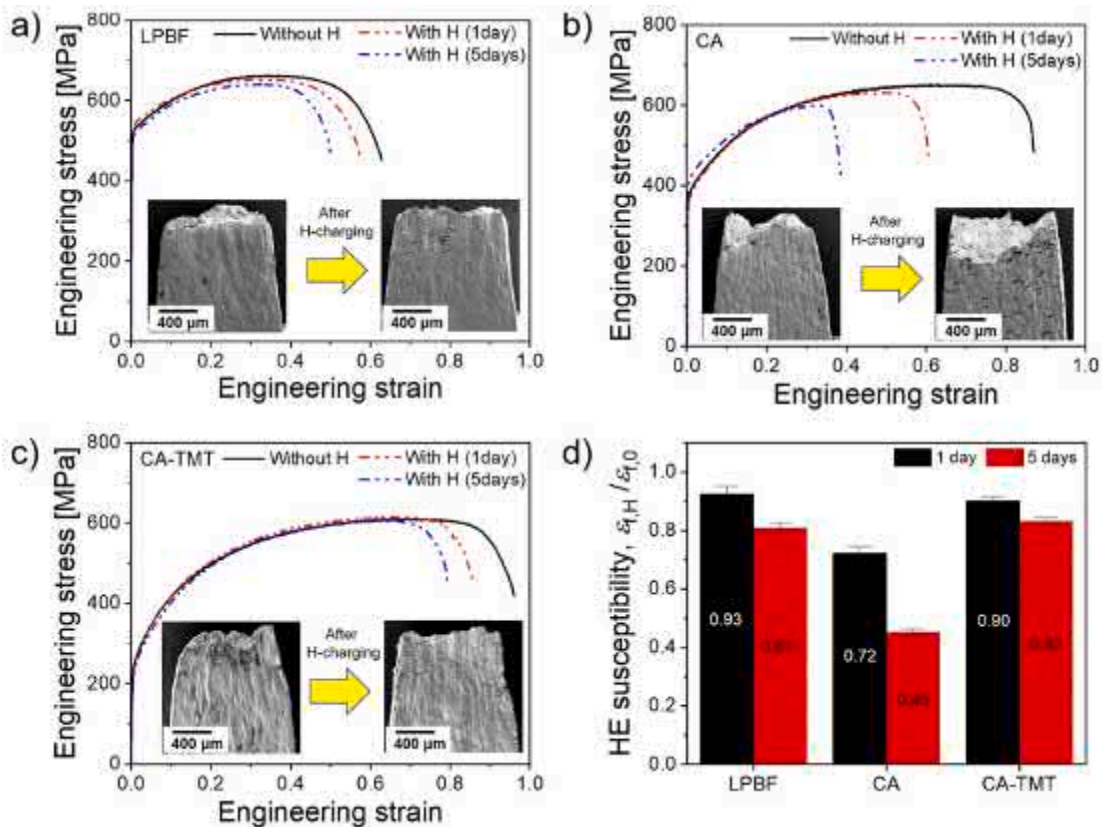
Fig. 4. Typical engineering stress-engineering strain curves of the (a) LPBF, (b) CA, and (c) CA-TMT samples with and without H. The insets show the SEM images of the surface of samples after tensile testing at the region of fracture. (d) Quantification of HE susceptibility for each condition. Error bars represent the standard deviations of the $\varepsilon_{f,H}/\varepsilon_{f,0}$ values obtained from several stress-strain curves. Note that tensile loading direction is parallel to the Y direction in Figs. 2 and 3. (LPBF: Laser powder-bed-fusion, CA: Casting plus annealing, TMT: Thermomechanical treatment).

the solidification cell structure which acts as an effective obstacle to dislocation motion [31,32]. However, the LPBF sample shows lower elongation to failure (~62%) than the other materials (~85% and ~96% for the CA and CA-TMT samples, respectively), which is attributed to the combined effects of the general trade-off between strength and ductility, the high dislocation density, and the presence of LPBF-induced defects like voids and pores [27,39,40]. Note that tensile loading direction is parallel to the Y direction in Figs. 2 and 3. Since no strong texture is developed along the direction of tensile loading, the possible effects from texture can be neglected. After H-charging for 1 day, the ductility of all 304L AASs gets reduced, as expected (Fig. 4). However, each sample exhibits different HE susceptibility: H-charging results in a significant loss in ductility for the case of the CA sample, whereas only a small effect of H on ductility is observed for the LPBF and CA-TMT samples. With further increasing H-charging time to 5 days, a larger loss in ductility was observed for all investigated samples, but the LPBF and CA-TMT samples are still less susceptible to HE than the CA sample. The HE susceptibility of a material is usually quantitatively represented as the ratio of the total elongation to failure of the H-charged sample ($\varepsilon_{f,H}$) to that of the uncharged sample ($\varepsilon_{f,0}$), i.e., $\varepsilon_{f,H}/\varepsilon_{f,0}$ [9,13]. As shown in Fig. 4d, the values of $\varepsilon_{f,H}/\varepsilon_{f,0}$ obtained from the CA-TMT and LPBF samples are obviously higher than those obtained from the CA sample. It is also noted that the H-charged CA sample shows a large number of cracks on the surface after tensile testing, but the CA-TMT and LPBF samples show relatively less H-assisted cracking (see insets in Fig. 4). These results suggest that, in the absence of retained δ, HE susceptibility of the LPBF sample is similar to that of the conventionally produced sample. HE in the present 304L ASSs is apparently related to the presence of retained δ. Considering the previous research by Baek et al. [34] which reported higher HE resistance in AM-processed 304L, it is interesting to note that the here observed HE susceptibility of the LPBF sample is similar to that of the conventionally produced sample in the absence of δ ferrite (CA-TMT sample). The possible reason for this inconsistency will be discussed in section 4.1.

The H contents in the samples after H-charging were measured by analyzing TDS curves, and the results are shown in Fig. 5. The inset of Fig. 5 displays the variation in H content with H-charging time for the LPBF sample, which suggests that H content increases with H-charging time. After 5 days of H-charging (main plot of Fig. 5), all samples show a single desorption peak at similar temperatures (~220 °C), indicating that the H trapping sites are similar in all present samples. In general,
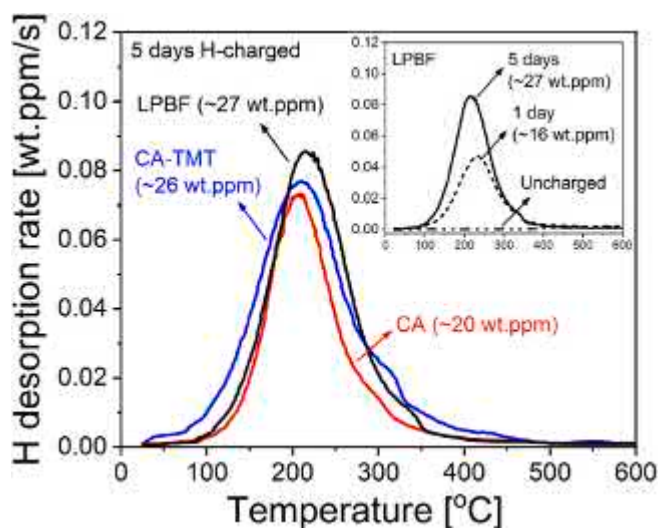
such a low-temperature peak corresponds to relatively weak H trapping sites such as interstitial lattice sites and weak H trapping defects such as dislocations and GBs [41–43]. It is also interesting to note that, although the LPBF sample contains a large fraction of low-angle grain boundaries and cellular walls, the total H content in the LPBF sample is very similar to that in the CA-TMT sample (see Fig. 5). In addition, despite showing a significant HE effect, the CA sample exhibits a slightly lower H content than the other samples. On this basis, we can conclude that the presence of low-angle grain boundaries and cellular walls has a negligible effect on the H content of the LPBF sample and, more importantly, the different HE susceptibilities of the present samples are not primarily related to their total H contents.

3.2. Deformation microstructure without the presence of H

With the aid of digital image correlation mapping, the evolution of the deformation microstructure in the uncharged samples was investigated by ECCI on different regions corresponding to different local strain levels (from ~5% up to ~40%). At a low strain of ~5%, deformation twins with two different twinning systems are observed (Fig. 6a) which are nucleated from high-angle grain boundaries and penetrate through the cellular walls. From the zoom-in image of 5% strained microstructure (middle of Fig. 6a), a large density of stacking faults can be observed within a cell, indicating that dislocation glide is mainly governed by partial dislocations, whose motion is impeded by cellular walls [32]. With increasing the strain to ~40%, a significant increase in the mechanical twin density is observed for both twinning systems.

In contrast, the CA sample shows a different microstructural evolution during deformation (Fig. 6b). A low strain of ~5% resulted in a substantial increase in the density of dislocations. At this stage, multiple intersecting planar slip lines are observed, suggesting that the plastic deformation mainly occurs by planar slip. We identified that the slip lines are along {111} planes by EBSD trace analysis. Upon increasing the strain level to ~20%, a well-developed dislocation cell structure is observed and some grains show mechanical twins with a thickness of a few nanometers. A further increase in the strain to ~40% leads to activation of two different twinning systems and a significant increase in mechanical twin density for both twinning systems. This observation is in agreement with prior reports on deformation mechanisms of conventional ASSs, i.e. the co-existence of dislocation slip and mechanical twinning [44–46]. The development of deformation microstructure in the CA-TMT sample was found to be similar to that in the CA sample, except for the absence of δ. Thus, only the results for the CA samples are displayed in Fig. 6.

These microstructure observations demonstrate that dislocation glide in the LPBF sample is more difficult compared to samples CA and CA-TMT due to the presence of the cellular structure and thus mechanical twinning was favored and activated already at an early stage of deformation. However, as shown in Fig. 6, there is no significant difference in the deformed microstructure between samples LPBF and CA (-TMT) at relatively high strain levels (above ~20%). This observation suggests that the intrinsic material properties such as the stacking fault energy may be similar for both samples, but that the critical stress for twinning is reached at an earlier stage of deformation in the LPBF sample because of its high yield stress resulting from the presence of the cellular structure. Another interesting observation is that the cellular structure in the LPBF sample remained stable during the entire deformation (Fig. 6a).

According to the values associated with the transformation $\Delta G^{\gamma \rightarrow \alpha}$, all investigated samples have a metastable austenitic matrix, which conforms to the presumption of a minimum driving force of −2.1 kJ/mol that is necessary for triggering deformation-induced martensitic transformation [47]. However, it is challenging for this material to distinguish strain-induced α′ martensite from the γ matrix in the ECCI images (see Fig. 6). Therefore, the microstructure evolution of the uncharged samples with increase in local strain from 20% to 60% was investigated
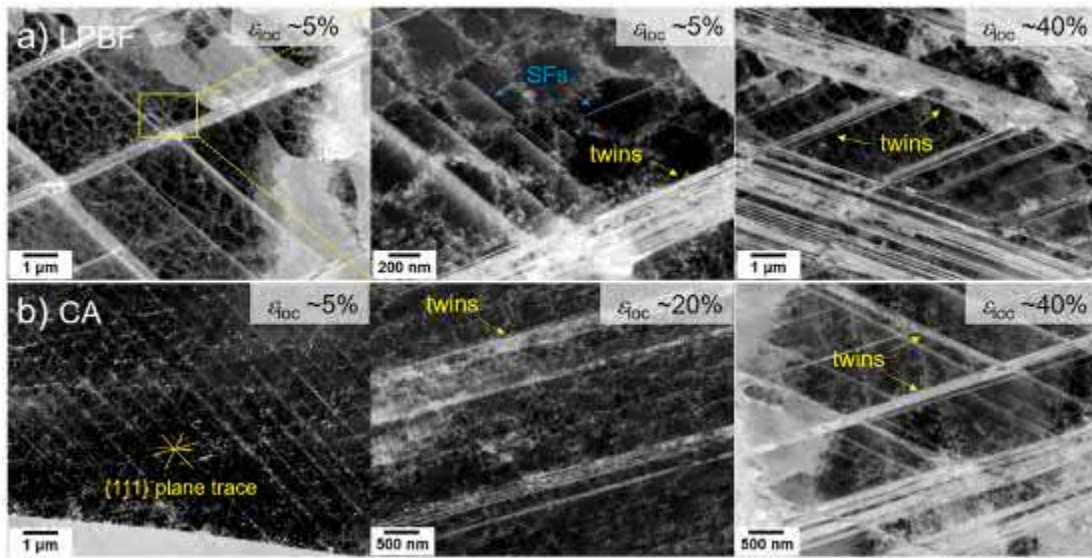

Fig. 5. H desorption curves of the 5 days H-charged samples at a heating rate of 26 °C/min. The inset shows the variation in H desorption curve with H-charging time for the LPBF sample. (LPBF: Laser powder-bed-fusion, CA: Casting plus annealing, TMT: Thermomechanical treatment).

Fig. 6. Deformation microstructure of the (a) LPBF and (b) CA samples revealed by ECCI at different strain levels. (LPBF: Laser powder-bed-fusion, CA: Casting plus annealing).

also by EBSD mapping. Fig. 7a-c display EBSD phase maps for the LPBF, CA, and CA-TMT samples, respectively. All samples exhibit similar nucleation behavior and distribution of α' martensite; rod-shaped α' martensite is mostly nucleated at the intersections of mechanical twins, and developed within the individual twins, which is in good agreement with previous studies on strain-induced martensitic transformation in ASSs (i.e., $\gamma \rightarrow$ twinning $\rightarrow \alpha'$) [21–24]. Although $\gamma \rightarrow \varepsilon \rightarrow \alpha'$ is another possible transformation sequence [21–24], α' martensite transformation in the present 304L ASSs most likely occurs in the sequence $\gamma \rightarrow$ twinning $\rightarrow \alpha'$ due to the substantially low $\Delta G^{\gamma \rightarrow \varepsilon}$ values (-0.50 kJ/mol). Interestingly, the volume fraction of α' ($f_{\alpha'}$) in the CA sample is much higher than that in the LPBF and CA-TMT samples at the same local strain. For example, $f_{\alpha'}$ at a local strain of 60% for the LPBF, CA, and CA-TMT samples are $\sim$3%, $\sim$16%, and $\sim$1%, respectively (Fig. 7). Note that the CA sample shows both δ and α', but δ can be distinguished from α' in terms of its blocky morphology (see Fig. 7b). It is interesting to note that, although all samples have similar $\Delta G^{\gamma \rightarrow \alpha}$ and M_{d30} values, the CA sample shows a much lower austenite stability than the other materials. In addition, there is no significant difference in mechanical stability of austenite between the LPBF and CA-TMT samples, which is inconsistent with results reported previously on AM-processed 304L steel [34,40]. The possible explanation for this unexpected behavior will be provided in section 4.1.

3.3. H-induced fracture and cracking

Fig. 8 shows high- and low-magnification fractographs of the tensile-tested specimens of the 5 days H-charged samples. Since H effects on ductility are more clearly apparent in the 5 days charged samples (especially for the LPBF and CA-TMT samples), the investigation of H-induced fracture and cracking was focused on the 5 days charged samples. The fracture surfaces of the H-charged specimens consist of two regions with distinctly different features. The central regions of the fracture surface show dimples (Fig. 8a₂,b₂,c₂), whereas the regions close to the side edges of the sample, where the material was exposed to H-charging, exhibit the characteristics of quasi-cleavage fracture (Fig. 8a₃, b₃,c₃). Generally, when electrochemical H charging is conducted, especially on FCC metals and samples which have a relatively low H diffusivity, H is highly concentrated near the charged surface and thus a H concentration gradient from the edge to the inner regions of the samples is induced [5,8]. For this reason, the quasi-cleavage fracture type observed at the specimen edges is attributed to the high H

concentration. An interesting feature can be found when comparing the H-induced brittle regions among the samples (Fig. 8a₃,b₃,c₃): the depth of the brittle region, i.e. the H-affected zone, in samples CA-TMT and LPBF is significantly shallower ($\sim$20–50 μm) than that in sample CA ($\sim$140–180 μm). This observation further supports that the CA-TMT and LPBF samples are less susceptible to HE than the CA sample. In the central region of the fracture surface, where the influence of H is negligible, the LPBF sample exhibits remarkably different features from the CA and CA-TMT samples: Considerably large voids/pores are spaced bout by regions covered by fine dimple. Since partially unmolten particles are frequently found within these large voids/pores, as indicated by the arrows in Fig. 8a₁, we assume that this feature may be caused by the presence of inherent defects such as unmolten particles and lack-of-fusion porosity in the LPBF sample [48,49].

To understand the H-assisted cracking behavior, cross-sections of the tensile-tested specimens were cut along the tensile direction and observed by optical microscopy first. Fig. 9 displays representative optical micrographs of the cross-sectional region in the tensile-tested sample.

Two important features are noteworthy in Fig. 9. First, only the H-charged samples show surface cracks propagating perpendicular to the tensile axis. Second, it is clear that the depth of these H-assisted cracks is much shallower in the LPBF and CA-TMT samples compared with the CA sample. Considering the similarity of H contents and H diffusivities among the samples (which will be discussed in section 4.3), this result suggests a lower resistance to H-assisted cracking in the CA sample. To identify the correlations between the microstructure and the crack propagation path, more detailed microstructural observations were conducted on the secondary cracks by means of EBSD measurements. Fig. 10a–c show the image quality map and the corresponding phase map for the H-charged CA, CA-TMT, and LPBF samples, respectively. It is revealed that all samples show similar H-assisted cracking behavior; the majority of cracks observed nucleate and propagate along the γ-α' interface (denoted γ-α' interface crack) as well as within α' (denoted α' crack) as indicated by white and blue arrows in Fig. 10, respectively. Rarely, H-assisted cracks are propagating through both γ and α'. A high magnification image of these cracks (Fig. 10a₃,b₃,c₃) suggests that these alternating cracks are formed by coalescence of several γ-α' interface cracks and α' cracks. In some cases, the cracks tend to initiate at the γ-α' interfaces (or within α') and propagate through the γ matrix, as indicated by the yellow arrows in Fig. 10. However, since the crack propagation through austenite only occurs in narrow γ layers between α' martensite
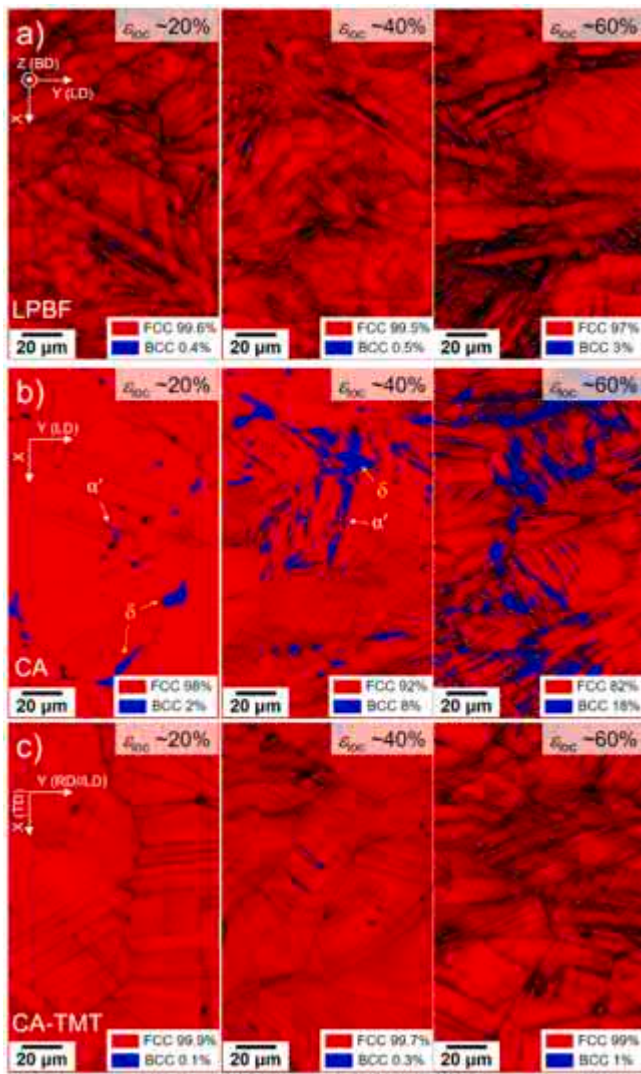
Fig. 7. EBSD phase map with the image quality map superimposed of the (a) LPBF, (b) CA, and (c) CA-TMT samples with increasing local strain from ~20% to ~60%. (EBSD step size: 100 nm, LPBF: Laser powder-bed-fusion, CA: Casting plus annealing, TMT: Thermomechanical treatment, RD: Rolling direction, TD: Transverse direction, LD: Loading direction).

regions as a coalescence process of α′-related cracks, it presumably has only a minor effect on the overall H-assisted cracking behavior. Thus, it is apparent that the strain-induced martensitic transformation plays an important role in H-assisted cracking for all types of samples.

4. Discussion

Results of the tensile experiments in Section 3 clearly demonstrate that HE in 304L ASS is apparently related not only to the presence of retained δ ferrite, but also to the amount of strain-induced α′ martensite. However, the role of δ ferrite in HE of ASSs still remains controversial, although it has been studied by many researchers [14,15,50,51]. Moreover, some studies reported that there was no significant effect of δ on HE when the amount of δ is less than 10% [15,50]. In this study, only ~1% retained δ is observed in sample CA, and regardless of the presence of δ, all investigated samples show similar H-assisted cracking behavior, i.e. cracks are initiated in the region where strain-induced martensitic transformation occurs. Even in the CA sample, H-assisted cracks are more likely formed near strain-induced α′ rather than inside the retained δ (see Fig. 10b$_2$). Thus, it can be suggested that strain-induced martensitic transformation is the primary factor controlling the HE susceptibility in 304L ASSs and the retained δ may partially contribute to this process.

Therefore, in the case of 304L ASS, it is important to achieve high austenite stability for likewise achieving a high HE resistance. For this purpose, 304L produced by conventional casting requires several thermomechanical treatments, whereas LPBF-processed 304L does not require any further processing steps. From this point of view, it can be concluded that the LPBF process itself leads to an enhanced strength in the ASS, and it also renders the sample less or equally susceptible to HE compared to conventionally produced 304L. In the following we discuss these results in terms of variations in mechanical stability of austenite, H-assisted cracking behavior, and H diffusion and trapping behavior.

4.1. Variations in mechanical stability of austenite

First, it is important to understand why the CA sample shows a much lower austenite stability than the others, because this observation deviates from what is expected from the $\Delta G^{\gamma \rightarrow \alpha}$ and M_{d30} values. Considering that $\Delta G^{\gamma \rightarrow \alpha}$ and M_{d30} values are calculated based on overall chemical composition, this inconsistency may arise from a possible local chemical inhomogeneity in the samples [18]. To check this possibility, the elemental distribution was analyzed by EDS elemental mapping (Fig. 11 and Fig. 12). The back-scattered electron (BSE) image and the corresponding EDS maps of the LPBF sample (Fig. 11a) indicate a homogeneous distribution of constituent elements on the micro-scale.
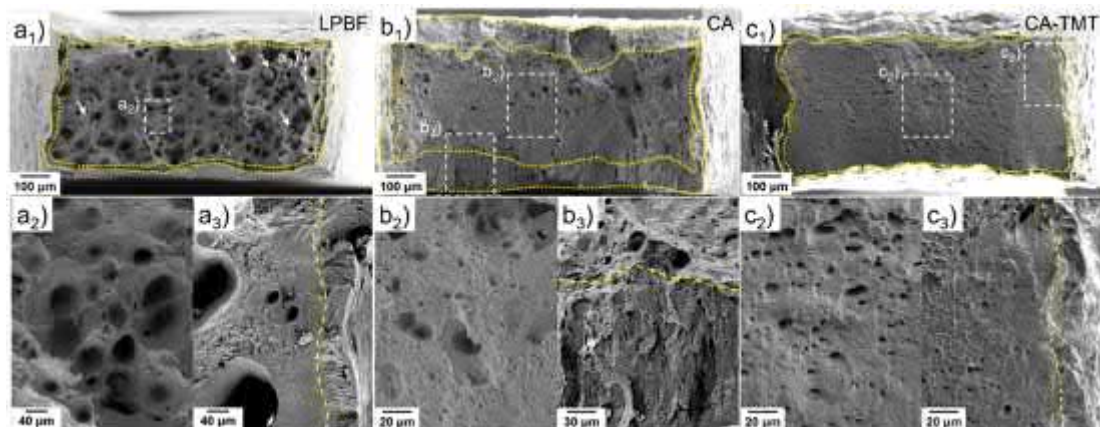

Fig. 8. The low- and high-magnification SEM images of the tensile fracture surfaces for the H-charged (a) LPBF, (b) CA, and (c) CA-TMT samples. (LPBF: Laser powder-bed-fusion, CA: Casting plus annealing, TMT: Thermomechanical treatment).
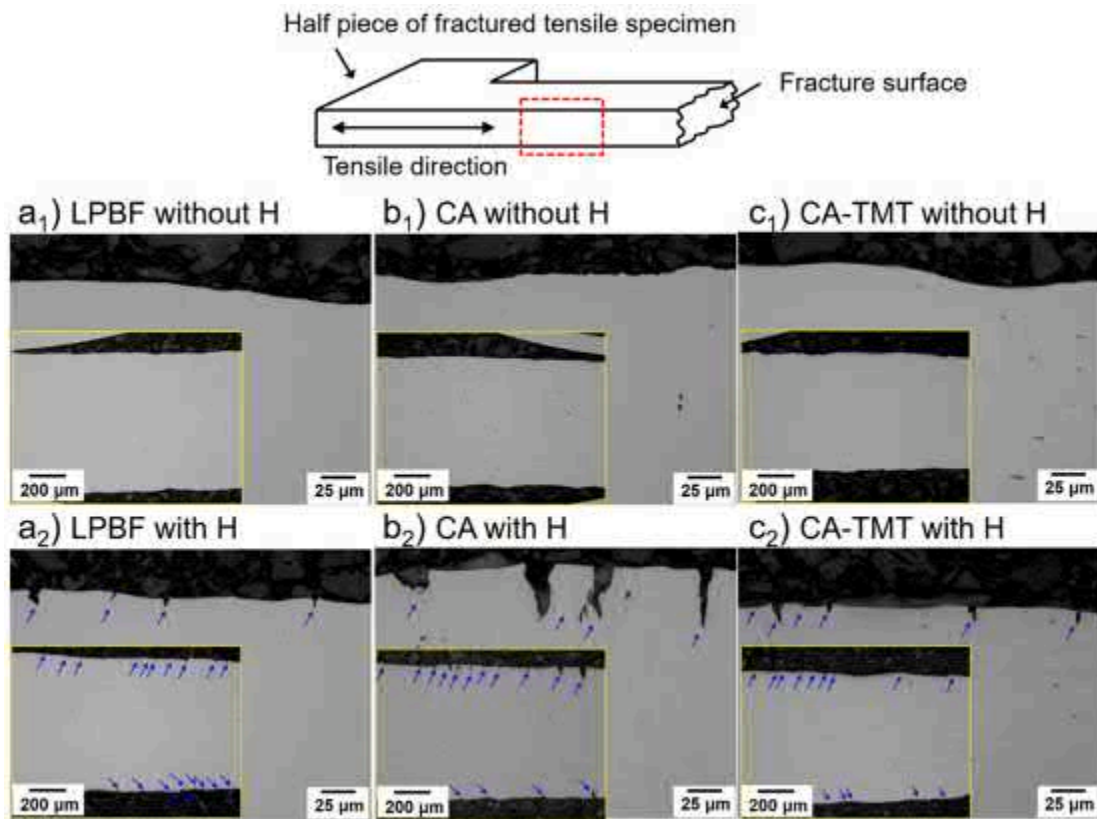
Fig. 9. Optical micrographs of the cross-sectional region in the tensile-tested sample with the insets showing the low-magnification images. The arrows indicate the H-assisted cracks. (LPBF: Laser powder-bed-fusion, CA: Casting plus annealing, TMT: Thermomechanical treatment).
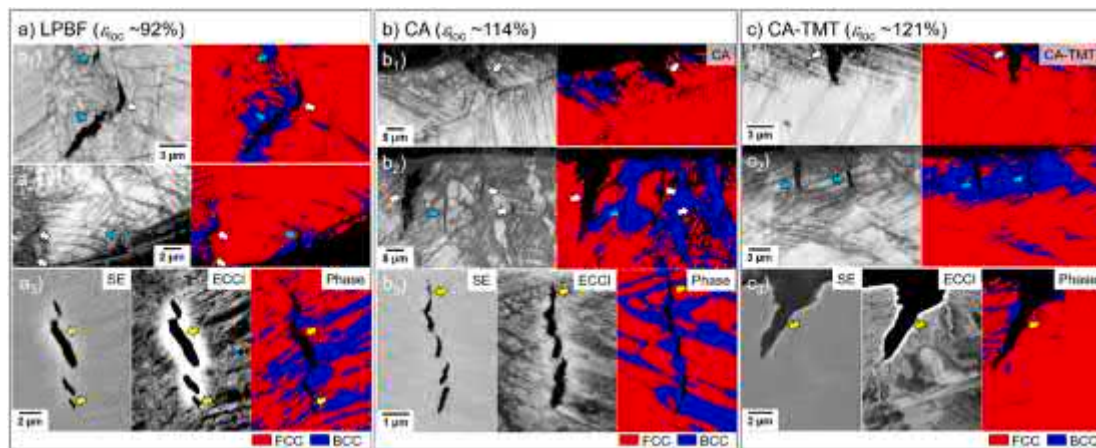

Fig. 10. Secondary H-assisted cracks in the (a) LPBF, (b) CA, and (c) CA-TMT samples: $(a_{1,2})$–$(c_{1,2})$ show the image quality maps and the corresponding phase distribution maps obtained from EBSD measurements around the H-assisted cracks; (a_3)–(c_3) show high magnification secondary electron (SE) images and the corresponding ECCI and EBSD phase map of the H-assisted cracks (EBSD step size: 50 nm). The white, blue and yellow arrows denote γ-α' interface cracks, α' cracks, and γ penetrating cracks, respectively. (LPBF: Laser powder-bed-fusion, CA: Casting plus annealing, TMT: Thermomechanical treatment). (For interpretation of the references to colour in this figure legend, the reader is referred to the Web version of this article.)

STEM annular dark field image shows a high density of the dislocation structure near the cell wall, however, we could not find any indication of elemental segregation from the STEM-EDS elemental mapping (Fig. 11b). Thus, we can conclude that the constituting elements are homogeneously distributed in the LPBF sample despite the presence of a cellular solidification substructure. This observation is in good agreement with the results obtained in rapid solidification experiments including splat quenching and laser welding which showed that a higher cooling rate leads to partitionless austenitic solidification [52]. Thus, the high characteristic cooling rate associated with the LPBF process results in a more homogeneous elemental distribution compared to the conventional processing routes encountered in commercial production of this steel. However, the EDS results of the CA sample (Fig. 12a) reveals that elemental partitioning between γ and δ is evident for Cr and Ni and, more importantly, the γ regions nearby δ are enriched in Cr but depleted in Ni. This clear chemical inhomogeneity observed in the γ matrix may be attributed to the incomplete partitioning of Cr and Ni to the γ that had transformed from the δ during casting. The detailed mechanism on this
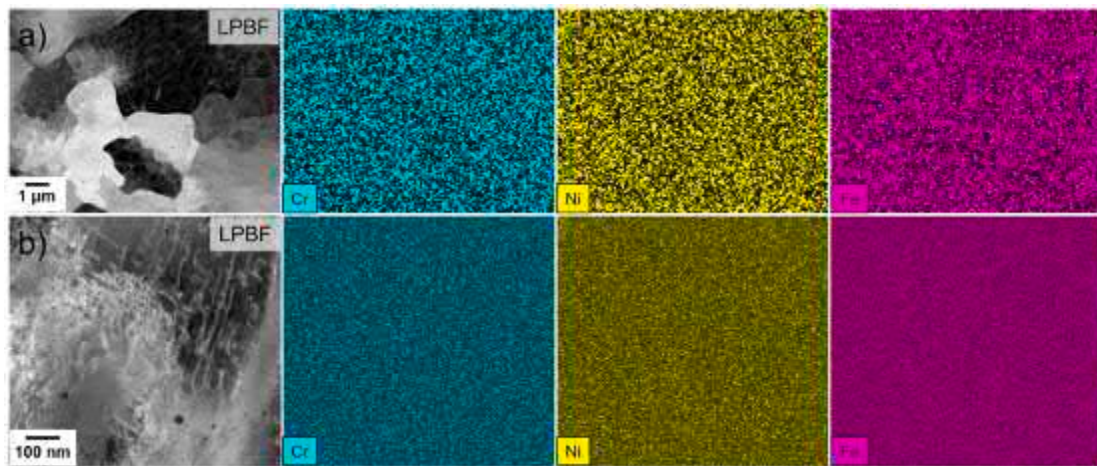
Fig. 11. Elemental distribution in the LPBF sample. (a) BSE image and the corresponding EDS maps and (b) STEM annular dark field image and the corresponding EDS maps. (LPBF: Laser powder-bed-fusion).
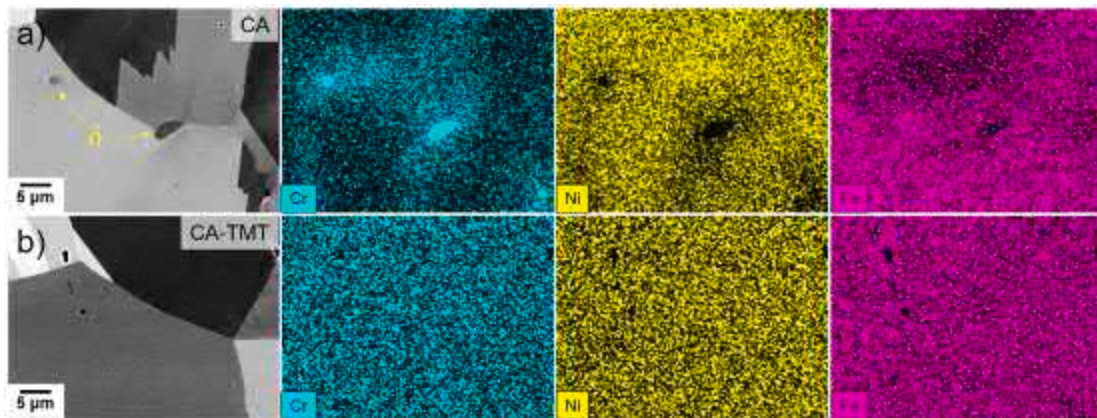

Fig. 12. BSE image and the corresponding EDS maps of the (a) CA and (b) CA-TMT samples. (CA: Casting plus annealing, TMT: Thermomechanical treatment).

phenomenon and its verification are provided in the Supplementary Material. Since a slight difference in chemical composition (especially Ni content) causes a substantial change in the mechanical stability of austenite and thus HE susceptibility [36,53], the γ region located close to δ-ferrite ($\sim$6.4 wt% Ni and $\sim$18.3 wt% Cr) would exhibit a lower austenite stability and thus lower HE resistance, compared to γ regions that are located far away from δ-ferrite ($\sim$8.8 wt% Ni and $\sim$16.2 wt% Cr). A quantitative measure of chemical composition of these regions is given in the Supplementary Material. In contrast to the CA sample, a homogeneous elemental distribution is observed in the CA-TMT sample (see Fig. 12b), suggesting that the imposed TMT completely eliminates

chemical inhomogeneity as well as δ from the CA sample, thus enhancing its austenite stability.

In addition to the chemical matrix inhomogeneity, it is often found in the deformed CA sample that strain (and the associated dislocation density) is localized at γ-δ interfaces, as shown in Fig. 13. Furthermore, Fig. 13 clearly shows that the microstrain (reflected by the density of dislocations) is more localized at the γ-δ interfaces rather than at the γ grain boundaries, suggesting that the γ-δ interfaces act as the sites of high strain localization. This result is consistent with the previous literatures in which δ ferrite was found to impede dislocation glide and promote dislocation pile ups at the γ-δ interfaces due to its strain
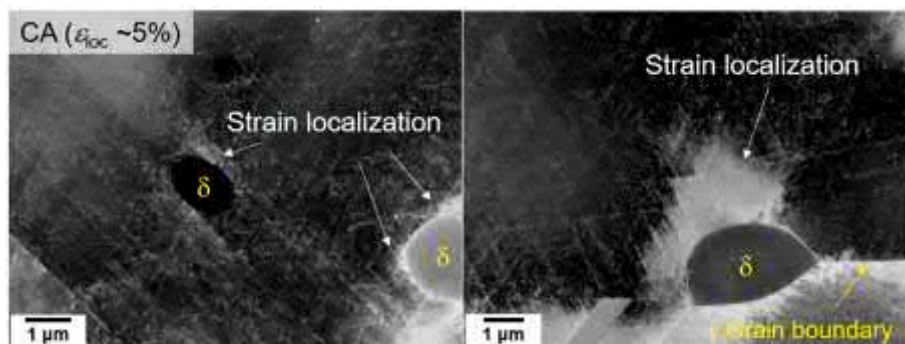
Fig. 13. ECCI images of the deformed CA sample showing strain localization near the retained δ. (CA: Casting plus annealing).

incompatibility between δ ferrite and γ matrix [54,55]. Since such dislocation pile-ups can reduce the energy barrier for strain-induced martensitic transformation [56], the increased density of dislocations near the γ-δ interfaces is expected to promote the formation of α′. Thus, a large volume fraction of α′ observed in the CA sample is mainly attributed to the chemical inhomogeneity-induced localized reduction of austenite stability, and the presence of retained δ-ferrite additionally contributes to the strain-induced martensitic transformation by inducing a high density of dislocations.

Another interesting feature is that although the LPBF sample clearly exhibits a cellular substructure in its initial state (after solidification), its austenite stability is similar to that of the CA-TMT sample. In fact, $f_{\alpha'}$ in the LPBF sample is slightly higher than that in the CA-TMT sample for all investigated strain levels (see Fig. 7). However, this is simply due to the fact that the driving force ($\Delta G^{\gamma \to \alpha}$) is slightly higher in the LPBF sample than that in the CA-TMT sample. Thus, we assume that neither nucleation nor growth of α′ is significantly affected by the presence of the solidification cell substructure. With regard to the growth of α′, one may argue that the solidification cell substructure in the LPBF sample may act as a barrier that hinders the growth of α′, given that this structure remains stable over the entire plastic deformation range probed here. However, this possibility can be readily ruled out because it is often found that the size of α′ martensite is bigger than that of the cellular substructure. The combined EBSD and ECCI observations of regions containing α′ martensite (Fig. 14) suggest that strain-induced α′ can easily pass through adjacent cells even at a relatively low strain level (e. g., ~20%). Since the dislocation cell walls are essentially low-angle grain boundaries (rather than high-angle grain boundaries), they are expected to have only a minor effect on suppressing the growth of α′ [23].

The results presented above are inconsistent with a previous study by Baek et al. [34], which reported a higher mechanical stability of austenite of AM-processed 304L compared to its conventionally produced reference counterpart. As mentioned above, the chemical composition (especially the Ni content) in ASS is very critical [36,53] and, indeed, AM-processed 304L steel can show higher mechanical stability of austenite when it contains higher Ni and N contents than conventionally produced 304L material [40]. Since the chemical compositions of the alloys were not provided in Ref. [34], a possibility that differences in chemical composition causes the difference in HE resistance cannot be excluded. By contrast, in the present study, we confirmed that the austenite stability of LPBF produced material is similar to that of conventionally produced samples in terms of the overall chemical composition, according to the calculated $\Delta G^{\gamma \to \alpha}$ and M_{d30} values. Therefore, the comparison between the LPBF and CA-TMT samples unambiguously reflects only the influence of the different features in the microstructure (rather than in the chemical composition) between additively and conventionally manufactured 304L ASSs, suggesting that the solidification cell structure in AM-processed 304L steel

has a negligible effect on the mechanical stability of the austenite. With this regard, we can conclude that the presence of δ ferrite and the inhomogeneous distribution of the alloying elements (especially Ni) in the γ matrix plays the most important role in determining the mechanical stability of austenite. Thus, the conventionally manufactured sample exhibits similar mechanical stability of austenite (or HE susceptibility) as the additively manufactured sample if both of them have similar $\Delta G^{\gamma \to \alpha}$ (or M_{d30}) values, fully austenite structure, and a homogeneous elemental distribution. To achieve this, 304L steel produced by conventional casting, may require several corresponding post-processing steps.

4.2. H-assisted cracking mechanism

4.2.1. Initiation of H-assisted cracking

Before identifying the mechanism of H-assisted crack initiation, the sequence of the H-assisted cracking processes should be discussed first, since one could argue that H-assisted cracks are first initiated within γ, and then the high strain localization near the crack tip promotes the martensitic transformation. However, considering that stresses are relaxed upon crack initiation, the microstructure in the vicinity of the crack initiation site (perpendicular to the crack propagation path) should represent the condition at the time of crack nucleation. In this study, the majority of crack initiation sites, which is typically located in the center of the crack, are identified as the γ-α′ interfaces and inside α′. Thus, it is likely that strain-induced martensitic transformation occurs prior to H-assisted cracking instead of being a result of cracking. More importantly, there is no evidence that H-assisted cracks and/or voids are initiated at the critical sites of γ, such as GBs and intersections of slip lines (or mechanical twins), as shown in ECCI images of Fig. 10. This supports our hypothesis that, at least for the present samples, strain-induced martensitic transformation occurs first, and then the regions containing α′ act as the crack initiation sites.

In fact, strain-induced martensitic transformation is a crucial factor for the severe HE of metastable ASS despite some dispute in the literature [9,43,57]. The general consensus is that the strain-induced martensite contributes strongly to H-assisted cracking [11,46,58], which can be explained as follows: in general, the body centered cubic (BCC) structure of α′ martensite is inherently more susceptible to H-assisted cracking than the FCC austenitic structure [9,10,53]. Furthermore, the H solubility in α′ martensite is lower than that in the austenite by one to two orders of magnitude [59]. Thus, when H-containing austenite is transformed to α′ martensite and the martensite inherits the H from the austenite, it suddenly exceeds the H solubility limit in α′ martensite, i.e. the H becomes excess H. Following the transformation, excess H diffuses to the surrounding austenite and accumulates at the γ-α′ interphase boundary, since the H diffusivity is much higher in α′ martensite than in austenite [59–61]. When a critical H concentration is attained at this boundary, H leads to decohesion of the
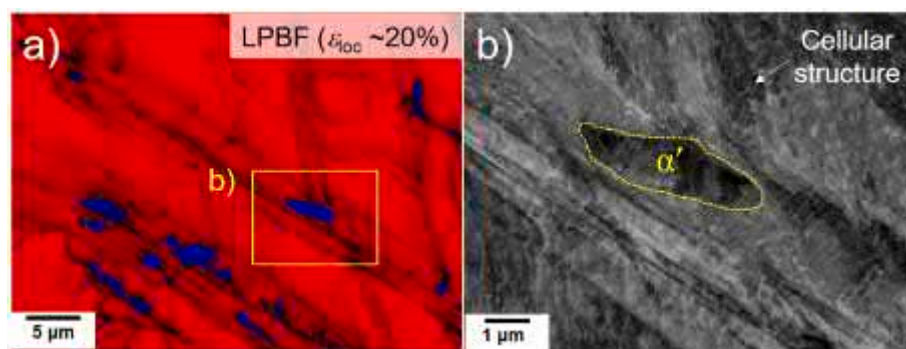

Fig. 14. Distribution of strain-induced α′ martensite in the LPBF sample strained to ~20%: (a) phase distribution map and (b) magnified ECCI image of a selected area highlighted in (a). (EBSD step size: 50 nm, LPBF: Laser powder-bed-fusion).

γ-α′ interphase boundary and thus cracks start to nucleate and propagate along this boundary (γ-α′ interface crack) [12,62,63]. Furthermore, H-enhanced slip localization in the retained γ can cause void formation [64,65] along the γ-α′ interface, further facilitating the decohesion process. Additionally, the excess H can also be accumulated within the substructure of α′ martensite (i.e., at lath/block boundaries). In this case, supersaturated H at lath/block boundaries might lead to decohesion and crack initiation/propagation within α′ martensite (α′ crack) [46,61,66, 67]. Since both, γ-α′ interface cracks and α′ cracks are frequently observed in Fig. 10, it seems that all mechanisms mentioned above are activated. Thus, the excess H resulting from the strain-induced α′ martensitic transformation plays a crucial role in HE of the present samples. In this regard, it can be concluded that the presence of the austenite with a low stability around retained δ-ferrite in the CA sample enhances the localized strain-induced α′ martensite transformation, which in turn leads to the formation of possible crack initiation sites in the presence of H, and thus contributes to the severe HE susceptibility.

4.2.2. Growth of H-assisted cracking

In addition to the crack initiation, the crack growth resistance is another crucial factor to control the elongation to failure in a H-providing environment; i.e., low resistance to crack growth results in brittle fracture at low strain levels. In this study, it was clearly observed that the CA sample shows a much higher number of deep H-assisted cracks than the other samples (Fig. 9), indicating that the CA sample exhibits a lower resistance to crack growth when exposed to a H-donating atmosphere.

H-assisted crack growth in ASSs has often been attributed to the coupled H diffusion and the increase in H concentration ahead of a crack tip [60,63,68]. Under tensile loading conditions, a stress field with a hydrostatic component is developed in front of a crack tip and thus the enrichment of H at a critical site ahead of the crack tip is promoted by stress-driven H diffusion [69–71]. When the accumulated H concentration exceeds a critical value near the crack tip, H leads to continuous crack growth (new cracks initiate and coalesce with the pre-existing crack) and finally causes the complete fracture of the material [72, 73]. Thus, it can be concluded that the acceleration in crack growth due to H depends on the rate at which the H is provided to the critical region ahead of crack tip and thus to the local H concentration. On the other hand, it might be reasonable to assume that H diffusion to a crack tip can be accelerated by the presence of α′ near the crack, due to the high diffusion rate of H in α′, often referred to as short-path diffusion mechanism [59,60]. Besides the pre-existing α′, fresh α′ can be formed in the stress field in front of the crack tip, leading to further enhancement of H diffusion [18,63] and providing a high local oversaturation of H. In fact, Wang et al. [63] investigated the influence of martensitic transformation in front of a crack tip on the H enrichment by means of finite element analysis. They reported that the enrichment of H in front of the crack tip is accelerated by about four orders of magnitude due to the presence of α′ at the crack tip. Since the amount of both pre-existing α′ and fresh α′ around the crack is dependent on the austenite stability, a correlation between the austenite stability and the capacity of H diffusion ahead of the crack can be derived. Based on this concept, a relationship between austenite stability and resistance to crack propagation can be derived, as schematically illustrated in Fig. 15. In the CA sample, which has locally a low austenite stability, a large amount of α′ near the H-assisted crack significantly accelerates the stress-driven H diffusion to the crack tip and thus leads to continuous crack growth (see Fig. 15a). On the other hand, in the LPBF and CA-TMT materials, which have a high austenite stability, the enrichment of H at the crack tip is not sufficient due to the small amount of α′, and thus the H-assisted cracks can be easily arrested (see Fig. 15b). We therefore conclude that in the CA sample, a high capacity of H diffusion towards the crack tip leads to the continuous growth of H-assisted cracks and thus further contributes to material's HE susceptibility. For the same reason, the depth of the H-affected brittle zone in the CA samples is significantly deeper than
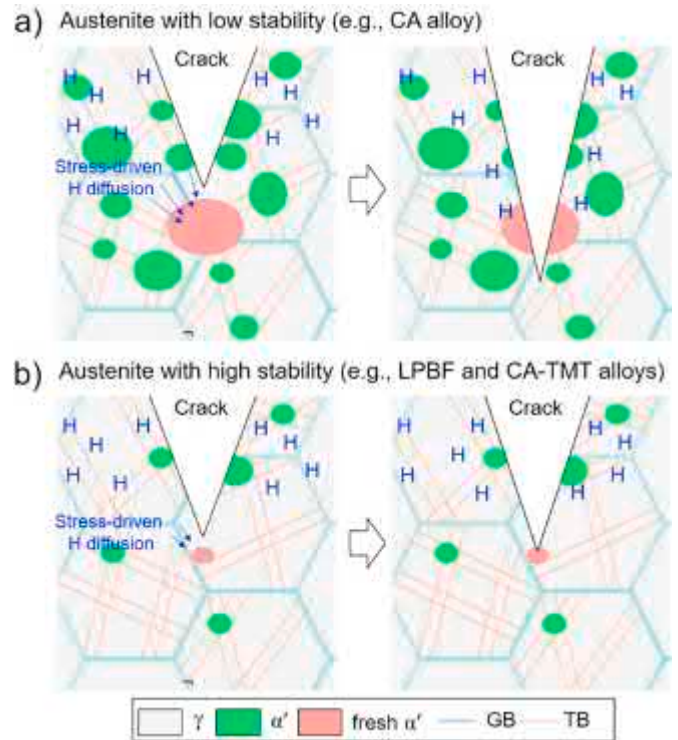

Fig. 15. Schematic illustration showing the influence of stress-driven H diffusion on crack growth resistance for austenite with (a) low stability and (b) high stability. Note that the shape of α′ is simplified as ellipsoid, but its actual shape is rodlike. (GB: Grain boundary, TB: Twin boundary).

that in the LPBF and CA-TMT specimens (Fig. 8).

4.3. Variations in H diffusion and trapping behavior

Since one may argue that the depth of a H-assisted crack (or H-affected brittle zone) is closely related to the H permeation depth after H-charging, it is instructive to investigate the possible difference in H permeation depth after H-charging among the investigated samples. Under the assumption that the H lattice diffusion follows Fick's law, the local H content, C_H, as a function of the depth from the surface, x, can be estimated as [74]:

$$C_H(x,t) = C_{Hs}\left[1 - erf\left(\frac{x}{2\sqrt{D_H t}}\right)\right] \qquad (2)$$

where C_{Hs} is the local H content at the surface of the H-charged samples, t is the charging time, and D_H is the diffusion coefficient of H. In Eq. (2), it is evident that when $x/(2\sqrt{D_H t}) \geq 2$, C_H approaches 0, hence, the maximum H permeation depth, x_{max}, after H-charging can be estimated by taking $x_{max}/(2\sqrt{D_H t}) = 2$, i.e., $x_{max} = 4\sqrt{D_H t}$. Since all samples were H-charged under the same conditions, x_{max} only depends on D_H. One could expect that the cell structure with a high dislocation density in the LPBF sample reduces the H diffusivity, since dislocations act as possible H trapping sites. However, in contrast to BCC metals, the increase in dislocation density has little influence on the apparent H diffusivity in ASSs [16,20,75], because the binding energy of H at dislocations in FCC metals is lower than the activation energy for H lattice diffusion, whereas in BCC metals the binding energy between H and the lattice dislocations is much higher than the activation energy for H lattice diffusion [20]. In this regard, D_H for all investigated samples can be assumed to be the same as that of 300-series ASS ($\sim 3.17 \times 10^{-16}$ m^2/s at RT [3]). By taking this D_H value, the x_{max} after 5 days H-charging can be estimated as $\sim$47 μm for all investigated samples. As shown in Figs. 8 and 9, however, a much higher depth of the H-affected brittle zone was

measured from the analysis of fracture surfaces in the CA sample (~180 μm). One may argue that the difference in chemical composition between the LPBF and CA(-TMT) samples leads to the different H diffusivities in them. However, it has been reported that the H diffusivity is not seriously affected by chemical composition in various ASSs and only varies from ~1.92×10^{-16} to ~4.28×10^{-16} m^2/s at room temperature [3]. Considering such range of variance in the H diffusivity, the estimated H diffusion depth can vary from ~36 to ~54 μm. Even if we consider this scatter on the estimated H diffusion depth, there is still a big discrepancy between the estimated H diffusion depth and the observed depth of ~180 μm of the H-affected brittle zone in the CA sample. The discrepancy between $x_{\max}$ and the depth of the H-affected brittle zone suggests that further permeation of H atoms occurs during the deformation. The reason for this may be the stress-driven H diffusion, as discussed in Section 4.2.2. From this viewpoint, it can be accepted that the depth of the H-affected brittle zone in the LPBF and CA-TMT samples is similar to the estimated $x_{\max}$, since both samples show a low capacity of H diffusion toward the crack tip. Note that the CA sample contains retained δ, but the amount of retained δ is too small to affect the H diffusion. Therefore, this observation further supports our hypothesis that stress-driven H diffusion towards the crack tip plays a crucial role in H-assisted crack growth. Although the motion of dislocations with trapped H can carry H deep into the material, thus assisting H transport [76,77], the shallow depth of the H-affected brittle zone in the LPBF and CA-TMT samples is similar to the estimated depth of H permeation. This implies that the movement of dislocations have a negligible effect on H diffusion in the present samples.

In contrast to the H diffusivity, the H content in ASSs increases with the density of dislocations, since dislocations provide additional H trapping sites [3,20]. However, TDS results in Fig. 5 reveal that the solidification cell substructure, which is decorated with dislocations, does not increase the H content of the LPBF sample significantly. Thus, it seems that, in contrast to the dislocations, the solidification cell structure may not provide additional H trapping sites and thus increase the H content. Although the detailed mechanism is not fully understood yet, it is reasonable to suggest that the low H trapping ability of the solidification cell structure is due to its low binding energy to H atoms. Since the solidification cell structure in the LPBF sample possesses a low-energy dislocation structure [31,78], the elastic stress field around this structure is different from that around the randomly distributed dislocations [79]. As a result, the binding energy of H to the solidification cell might also be different from that of randomly distributed dislocations. However, it is not feasible to investigate the influence of the solidification cell structure on the activation energy for H desorption under the present experimental conditions. For example, the TDS results in Fig. 5 show only one low-temperature peak, but there is a possibility that several peaks, which correspond to various weak H trapping sites such as grain boundaries and dislocations, may be overlapping. Therefore, additional systematic experiments and simulations are required to confirm the present trend and to provide information on the precise mechanism of the low H trapping ability of the solidification cell structure.

Before closing, it is constructive to address the issue that the H content in the CA sample is slightly lower than that in the CA-TMT sample. This phenomenon can be strongly correlated with the microstructure differences between them. As shown in the EDS map in Fig. 12, the Cr is highly concentrated inside and near the δ ferrite in the CA sample. Therefore, the austenite Cr content is much lower in the CA sample than that in the CA-TMT sample. Since Cr enhances H solubility [3,8], such depletion of Cr in the matrix austenite phase, accompanied by the δ ferrite in which the solubility of H is at least an order of magnitude lower than that in austenite [59], probably contribute to the slightly lower H content in the CA sample.

5. Conclusions

In the present study, H effects on tensile ductility of 304L ASS fabricated by laser powder-bed-fusion (LPBF) were systematically investigated through a series of tensile tests, microstructural analyses and by comparing the results with those of conventionally produced 304L ASSs (i.e., cast and annealed (CA) and cast, annealed and thermomechanically-treated (CA-TMT) samples). The major conclusions of this investigation are as follows:

1. Hydrogen embrittlement susceptibility of 304L ASSs varied with different production routes; H-charging resulted in a significant loss in ductility for the CA sample, whereas only a small effect of H on ductility was observed for the LPBF and CA-TMT samples. In the EBSD analysis, the volume fraction of strain-induced α′ martensite was higher in the CA sample (~16%) than in the LPBF and CA-TMT samples (~3% and ~1%, respectively) at the same strain level of 60%, suggesting that the low local mechanical stability of austenite may be the reason for the low resistance to hydrogen embrittlement in the CA sample.
2. The low mechanical stability of austenite in the CA sample can be explained by the presence of chemical inhomogeneity in austenite regions particularly around the retained δ zones in the initial state. Thermomechanical treatment, subsequent to CA, enhanced the chemical homogeneity, which in turn can effectively recover the austenite's stability and thus the resistance to hydrogen embrittlement in the CA-TMT sample.
3. In contrast, the LPBF sample showed a fully austenitic structure with homogeneous distributions of its constituent elements and a highly complex microstructure containing a characteristic solidification cellular structure due to the high solidification and cooling rates. These features led not only to enhanced strength but also to a high resistance to hydrogen embrittlement in the ASS without any further processing step.
4. In all samples, most of the H-assisted cracks were initiated at regions with α′ martensite, which further supports the critical role of strain-induced α′ martensitic transformation in hydrogen embrittlement of the present samples. Thus, it was revealed that the presence of δ and the chemical inhomogeneity inside γ matrix promoted hydrogen embrittlement by enhancing the deformation-induced martensitic transformation and the associated H enrichment at the γ-α′ interface.
5. The LPBF sample, in spite of the presence of a solidification cellular structure, showed similar HE susceptibility to the CA-TMT sample. This can be rationalized by the negligible effect of the solidification cell structure on austenite stability as well as on H trapping behavior.

Data availability statement

The raw/processed data that support the findings of this study are available from the corresponding authors on reasonable request.

CRediT authorship contribution statement

Declaration of competing interest

The authors declare that they have no known competing financial interests or personal relationships that could have appeared to influence

the work reported in this paper.

Acknowledgements

The research of D.-H. Lee was supported in part by research fund of Chungnam National University, and in part by Korean Institute for Advancement of Technology (KIAT) grant funded by the Korean Government (MOTIE, P0002019, The Competency Development Program for Industry Specialist). The authors would like to gratefully acknowledge P. Beley for the help of TDS analysis and the kind support of M. Nellessen, K. Angenendt, and M. Adamek at the Max-Planck-Institut für Eisenforschung.

Appendix A. Supplementary data

Supplementary data to this article can be found online at https://doi. org/10.1016/j.msea.2020.140499.

References

[1] M.R. Louthan, R.G. Derrick, Hydrogen transport in austenitic stainless steel, Corrosion Sci. 15 (1975) 565–577, https://doi.org/10.1016/0010-938X(75) 90022-0.

[2] T.-P. Perng, M. Johnson, C.J. Altstetter, Influence of plastic deformation on hydrogen diffusion and permeation in stainless steels, Acta Metall. 37 (1989) 3393–3397, https://doi.org/10.1016/0001-6160(89)90211-3.

[3] C.S. Marchi, B.P. Somerday, S.L. Robinson, Permeability, solubility and diffusivity of hydrogen isotopes in stainless steels at high gas pressures, Int. J. Hydrogen Energy 32 (2007) 100–116, https://doi.org/10.1016/j.ijhydene.2006.05.008.

[4] J.P. Hirth, Effects of hydrogen on the properties of iron and steel, Metall. Trans. 11 (1980) 861–890, https://doi.org/10.1007/BF02654700.

[5] H.K. Birnbaum, P. Sofronis, Hydrogen-enhanced localized plasticity—a mechanism for hydrogen-related fracture, Mater. Sci. Eng. 176 (1994) 191–202, https://doi. org/10.1016/0921-5093(94)90975-X.

[6] A. Barnoush, H. Vehoff, Recent developments in the study of hydrogen embrittlement: hydrogen effect on dislocation nucleation, Acta Mater. 58 (2010) 5274–5285, https://doi.org/10.1016/j.actamat.2010.05.057.

[7] I.M. Robertson, P. Sofronis, A. Nagao, M.L. Martin, S. Wang, D.W. Gross, K. E. Nygren, Hydrogen embrittlement understood, Metall. Mater. Trans. 46 (2015) 2323–2341, https://doi.org/10.1007/s11661-015-2836-1.

[8] Y. Zhao, D.H. Lee, M.Y. Seok, J.A. Lee, M.P. Phaniraj, J.Y. Suh, H.Y. Ha, J.Y. Kim, U. Ramamurty, J. il Jang, Resistance of CoCrFeMnNi high-entropy alloy to gaseous hydrogen embrittlement, Scripta Mater. 135 (2017) 54–58, https://doi.org/ 10.1016/j.scriptamat.2017.03.029.

[9] G. Han, J. He, S. Fukuyama, K. Yokogawa, Effect of strain-induced martensite on hydrogen environment embrittlement of sensitized austenitic stainless steels at low temperatures, Acta Mater. 46 (1998) 4559–4570, https://doi.org/10.1016/S1359-6454(98)00136-0.

[10] T. Michler, J. Naumann, Hydrogen environment embrittlement of austenitic stainless steels at low temperatures, Int. J. Hydrogen Energy 33 (2008) 2111–2122, https://doi.org/10.1016/j.ijhydene.2008.02.021.

[11] C. San Marchi, T. Michler, K.A. Nibur, B.P. Somerday, On the physical differences between tensile testing of type 304 and 316 austenitic stainless steels with internal hydrogen and in external hydrogen, Int. J. Hydrogen Energy 35 (2010) 9736–9745, https://doi.org/10.1016/j.ijhydene.2010.06.018.

[12] Y. Mine, K. Koga, O. Kraft, K. Takashima, Mechanical characterisation of hydrogen-induced quasi-cleavage in a metastable austenitic steel using micro-tensile testing, Scripta Mater. 113 (2016) 176–179, https://doi.org/10.1016/j. scriptamat.2015.11.013.

[13] L. Zhang, Z. Li, J. Zheng, Y. Zhao, P. Xu, C. Zhou, X. Li, Effect of strain-induced martensite on hydrogen embrittlement of austenitic stainless steels investigated by combined tension and hydrogen release methods, Int. J. Hydrogen Energy 38 (2013) 8208–8214, https://doi.org/10.1016/j.ijhydene.2013.01.198.

[14] J.A. Brooks, A.J. West, A.W. Thompson, Effect of weld composition and microstructure on hydrogen assisted fracture of austenitic stainless steels, Metall. Trans. 14 (1983) 75–84, https://doi.org/10.1007/BF02643740.

[15] J.R. Buckley, D. Hardie, The effect of pre-straining and δ-ferrite on the embrittlement of 304L stainless steel by hydrogen, Corrosion Sci. 34 (1993) 93–107, https://doi.org/10.1016/0010-938X(93)90261-E.

[16] Y. Wang, X. Wang, J. Gong, L. Shen, W. Dong, Hydrogen embrittlement of catholically hydrogen-precharged 304L austenitic stainless steel: effect of plastic pre-strain, Int. J. Hydrogen Energy 39 (2014) 13909–13918, https://doi.org/ 10.1016/j.ijhydene.2014.04.122.

[17] Y. Mine, N. Horita, Z. Horita, K. Takashima, Effect of ultrafine grain refinement on hydrogen embrittlement of metastable austenitic stainless steel, Int. J. Hydrogen Energy 42 (2017) 15415–15425, https://doi.org/10.1016/j.ijhydene.2017.04.249.

[18] G. Egels, L. Mujica Roncery, R. Fussik, W. Theisen, S. Weber, Impact of chemical inhomogeneities on local material properties and hydrogen environment embrittlement in AISI 304L steels, Int. J. Hydrogen Energy 43 (2018) 5206–5216, https://doi.org/10.1016/j.ijhydene.2018.01.062.

[19] Y.H. Fan, B. Zhang, J.Q. Wang, E.-H. Han, W. Ke, Effect of grain refinement on the hydrogen embrittlement of 304 austenitic stainless steel, J. Mater. Sci. Technol. 35 (2019) 2213–2219, https://doi.org/10.1016/j.jmst.2019.03.043.

[20] Y. Mine, C. Narazaki, K. Murakami, S. Matsuoka, Y. Murakami, Hydrogen transport in solution-treated and pre-strained austenitic stainless steels and its role in hydrogen-enhanced fatigue crack growth, Int. J. Hydrogen Energy 34 (2009) 1097–1107, https://doi.org/10.1016/j.ijhydene.2008.11.018.

[21] G.B. Olson, M. Cohen, A mechanism for the strain-induced nucleation of martensitic transformation, J. Less Common. Met. 28 (1972) 107–118, https://doi. org/10.1255/ejms.974.

[22] K. Spencer, M. Véron, K. Yu-Zhang, J.D. Embury, The strain induced martensite transformation in austenitic stainless steels: Part 1 – influence of temperature and strain history, Mater. Sci. Technol. 25 (2009) 7–17, https://doi.org/10.1179/ 174328408X293603.

[23] T. Masumura, N. Nakada, T. Tsuchiyama, S. Takaki, T. Koyano, K. Adachi, The difference in thermal and mechanical stabilities of austenite between carbon- and nitrogen-added metastable austenitic stainless steels, Acta Mater. 84 (2015) 330–338, https://doi.org/10.1016/j.actamat.2014.10.041.

[24] Y. Tian, A. Borgenstam, P. Hedström, Comparing the deformation-induced martensite transformation with the athermal martensite transformation in Fe-Cr-Ni alloys, J. Alloys Compd. 766 (2018) 131–139, https://doi.org/10.1016/j. jallcom.2018.06.326.

[25] D. Herzog, V. Seyda, E. Wycisk, C. Emmelmann, Additive manufacturing of metals, Acta Mater. 117 (2016) 371–392, https://doi.org/10.1016/j.actamat.2016.07.019.

[26] B.H. Jared, M.A. Aguilo, L.L. Beghini, B.L. Boyce, B.W. Clark, A. Cook, B.J. Kaehr, J. Robbins, Additive manufacturing: toward holistic design, Scripta Mater. 135 (2017) 141–147, https://doi.org/10.1016/j.scriptamat.2017.02.029.

[27] T. DebRoy, H.L. Wei, J.S. Zuback, T. Mukherjee, J.W. Elmer, J.O. Milewski, A. M. Beese, A. Wilson-Heid, A. De, W. Zhang, Additive manufacturing of metallic components – process, structure and properties, Prog. Mater. Sci. 92 (2018) 112–224, https://doi.org/10.1016/j.pmatsci.2017.10.001.

[28] E.A. Jägle, P.-P. Choi, J. Van Humbeeck, D. Raabe, Precipitation and austenite reversion behavior of a maraging steel produced by selective laser melting, J. Mater. Res. 29 (2014) 2072–2079, https://doi.org/10.1557/jmr.2014.204.

[29] E.O. Olakanmi, R.F. Cochrane, K.W. Dalgarno, A review on selective laser sintering/melting (SLS/SLM) of aluminium alloy powders: processing, microstructure, and properties, Prog. Mater. Sci. 74 (2015) 401–477, https://doi. org/10.1016/j.pmatsci.2015.03.002.

[30] P. Kürnsteiner, M.B. Wilms, A. Weisheit, P. Barriobero-Vila, E.A. Jägle, D. Raabe, Massive nanoprecipitation in an Fe-19Ni-xAl maraging steel triggered by the intrinsic heat treatment during laser metal deposition, Acta Mater. 129 (2017) 52–60, https://doi.org/10.1016/j.actamat.2017.02.069.

[31] Y.M. Wang, T. Voisin, J.T. McKeown, J. Ye, N.P. Calta, Z. Li, Z. Zeng, Y. Zhang, W. Chen, T.T. Roehling, R.T. Ott, M.K. Santala, P.J. Depond, M.J. Matthews, A. V. Hamza, T. Zhu, Additively manufactured hierarchical stainless steels with high strength and ductility, Nat. Mater. 17 (2018) 63–70, https://doi.org/10.1038/ NMAT5021.

[32] L. Liu, Q. Ding, Y. Zhong, J. Zou, J. Wu, Y.L. Chiu, J. Li, Z. Zhang, Q. Yu, Z. Shen, Dislocation network in additive manufactured steel breaks strength–ductility trade-off, Mater. Today 21 (2018) 354–361, https://doi.org/10.1016/j. mattod.2017.11.004.

[33] K. Saeidi, X. Gao, F. Lofaj, L. Kvetková, Z.J. Shen, Transformation of austenite to duplex austenite-ferrite assembly in annealed stainless steel 316L consolidated by laser melting, J. Alloys Compd. 633 (2015) 463–469, https://doi.org/10.1016/j. jallcom.2015.01.249.

[34] S. Baek, E.J. Song, J.H. Kim, M. Jung, U.B. Baek, S.H. Nahm, Hydrogen embrittlement of 3-D printing manufactured austenitic stainless steel part for hydrogen service, Scripta Mater. 130 (2017) 87–90, https://doi.org/10.1016/j. scriptamat.2016.11.020.

[35] K. Nohara, Y. Ono, N. Ohashi, Composition and grain size dependencies of strain-induced martensitic transformation in metastable Austenitic stainless steels, Tetsu-To-Hagane 63 (1977) 772–782, https://doi.org/10.2355/tetsutohagane1955.63.5_ 772.

[36] C. Izawa, S. Wagner, M. Deutges, M. Martín, S. Weber, R. Pargeter, T. Michler, H.-H. Uchida, R. Gemma, A. Pundt, Relationship between hydrogen embrittlement and Md30 temperature: prediction of low-nickel austenitic stainless steel's resistance, Int. J. Hydrogen Energy 44 (2019) 25064–25075, https://doi.org/ 10.1016/j.ijhydene.2019.07.179.

[37] K.G. Prashanth, J. Eckert, Formation of metastable cellular microstructures in selective laser melted alloys, J. Alloys Compd. 707 (2017) 27–34, https://doi.org/ 10.1016/j.jallcom.2016.12.209.

[38] S. Kou, Welding Metallurgy, second ed., 2003, https://doi.org/10.1016/j. theochem.2007.07.017.

[39] H.D. Carlton, A. Haboub, G.F. Gallegos, D.Y. Parkinson, A.A. MacDowell, Damage evolution and failure mechanisms in additively manufactured stainless steel, Mater. Sci. Eng. 651 (2016) 406–414, https://doi.org/10.1016/j. msea.2015.10.073.

[40] Z. Wang, T.A. Palmer, A.M. Beese, Effect of processing parameters on microstructure and tensile properties of austenitic stainless steel 304L made by directed energy deposition additive manufacturing, Acta Mater. 110 (2016) 226–235, https://doi.org/10.1016/j.actamat.2016.03.019.

[41] W.Y. Choo, J.Y. Lee, Thermal analysis of trapped hydrogen in pure iron, Metall. Trans. 13 (1982) 135–140, https://doi.org/10.1007/BF02642424.

[42] K.H. So, J.S. Kim, Y.S. Chun, K.-T. Park, Y.-K. Lee, C.S. Lee, Hydrogen delayed fracture properties and internal hydrogen behavior of a Fe–18Mn–1.5Al–0.6C

TWIP steel, ISIJ Int. 49 (2009) 1952–1959, https://doi.org/10.2355/isijinternational.49.1952.

[43] J.H. Ryu, Y.S. Chun, C.S. Lee, H.K.D.H. Bhadeshia, D.W. Suh, Effect of deformation on hydrogen trapping and effusion in TRIP-assisted steel, Acta Mater. 60 (2012) 4085–4092, https://doi.org/10.1016/j.actamat.2012.04.010.

[44] Y.F. Shen, X.X. Li, X. Sun, Y.D. Wang, L. Zuo, Twinning and martensite in a 304 austenitic stainless steel, Mater. Sci. Eng. 552 (2012) 514–522, https://doi.org/10.1016/j.msea.2012.05.080.

[45] P.M. Ahmedabadi, V. Kain, A. Agrawal, Modelling kinetics of strain-induced martensite transformation during plastic deformation of austenitic stainless steel, Mater. Des. 109 (2016) 466–475, https://doi.org/10.1016/j.matdes.2016.07.106.

[46] T. Michler, E. Bruder, Local strains in 1.4301 austenitic stainless steel with internal hydrogen, Mater. Sci. Eng. 725 (2018) 447–455, https://doi.org/10.1016/j.msea.2018.04.011.

[47] A. Borgenstam, M. Hillert, Driving force for f.c.c. → b.c.c. martensites in Fe-X alloys, Acta Mater. 45 (1997) 2079–2091, https://doi.org/10.1016/S1359-6454(96)00308-4.

[48] R. Casati, J. Lemke, M. Vedani, Microstructure and fracture behavior of 316L austenitic stainless steel produced by selective laser melting, J. Mater. Sci. Technol. 32 (2016) 738–744, https://doi.org/10.1016/j.jmst.2016.06.016.

[49] D. Sun, D. Gu, K. Lin, J. Ma, W. Chen, J. Huang, X. Sun, M. Chu, Selective laser melting of titanium parts: influence of laser process parameters on macro- and microstructures and tensile property, Powder Technol. 342 (2019) 371–379, https://doi.org/10.1016/j.powtec.2018.09.090.

[50] J.A. Brooks, A.J. West, Hydrogen induced ductility losses in austenitic stainless steel welds, Metall. Trans. (1981), https://doi.org/10.1007/BF02655194.

[51] W. Tyson, Embrittlement of types 316l and 347 weld overlay by post-weld heat treatment and hydrogen, Metall. Trans. 15 (1984) 1475–1484, https://doi.org/10.1007/BF02648577.

[52] J.M. Vitek, A. Dasgupta, S.A. David, Microstructural modification OF austenitic stainless steels BY rapid solidification, Metall. Trans. Phys. Metall. Mater. Sci. (1983), https://doi.org/10.1007/BF02645553.

[53] L. Zhang, M. Wen, M. Imade, S. Fukuyama, K. Yokogawa, Effect of nickel equivalent on hydrogen gas embrittlement of austenitic stainless steels based on type 316 at low temperatures, Acta Mater. 56 (2008) 3414–3421, https://doi.org/10.1016/j.actamat.2008.03.022.

[54] B.S. Rho, H.U. Hong, S.W. Nam, The fatigue crack initiation at the interface between matrix and δ-ferrite in 304L stainless steel, Scripta Mater. 39 (1998) 1407–1412, https://doi.org/10.1016/S1359-6462(98)00327-3.

[55] B. Rho, The effect of δ-ferrite on fatigue cracks in 304L steels, Int. J. Fatig. 22 (2000) 683–690, https://doi.org/10.1016/S0142-1123(00)00043-8.

[56] D.A. Porter, K.E. Easterling, M.Y. Sherif, Phase Transformations in Metals and Alloys, third ed., CRC Press, 2009 https://doi.org/10.1201/9781439883570.

[57] Y.S. Kim, S.H. Bak, S.S. Kim, Effect of strain-induced martensite on tensile properties and hydrogen embrittlement of 304 stainless steel, Metall. Mater. Trans. 47 (2016) 222–230, https://doi.org/10.1007/s11661-015-3198-4.

[58] T. Kanezaki, C. Narazaki, Y. Mine, S. Matsuoka, Y. Murakami, Effects of hydrogen on fatigue crack growth behavior of austenitic stainless steels, Int. J. Hydrogen Energy 33 (2008) 2604–2619, https://doi.org/10.1016/j.ijhydene.2008.02.067.

[59] Y. Mine, Z. Horita, Y. Murakami, Effect of hydrogen on martensite formation in austenitic stainless steels in high-pressure torsion, Acta Mater. 57 (2009) 2993–3002, https://doi.org/10.1016/j.actamat.2009.03.006.

[60] Y. Murakami, T. Kanezaki, Y. Mine, S. Matsuoka, Hydrogen embrittlement mechanism in fatigue of austenitic stainless steels, Metall. Mater. Trans. 39 (2008) 1327–1339, https://doi.org/10.1007/s11661-008-9506-5.

[61] B. Sun, W. Krieger, M. Rohwerder, D. Ponge, D. Raabe, Dependence of hydrogen embrittlement mechanisms on microstructure-driven hydrogen distribution in

[62] medium Mn steels, Acta Mater. 183 (2020) 313–328, https://doi.org/10.1016/j.actamat.2019.11.029.

[62] R.A. Oriani, P.H. Josephic, Equilibrium aspects of hydrogen-induced cracking of steels, Acta Metall. 22 (1974) 1065–1074, https://doi.org/10.1016/0001-6160(74)90061-3.

[63] Y. Wang, X.L. Li, D. Dou, L. Shen, J. Gong, FE analysis of hydrogen diffusion around a crack tip in an austenitic stainless steel, Int. J. Hydrogen Energy 41 (2016) 6053–6063, https://doi.org/10.1016/j.ijhydene.2016.03.003.

[64] M. Nagumo, Advances in physical metallurgy and processing of steels. Function of hydrogen in embrittlement of high-strength steels, ISIJ Int. 41 (2001) 590–598, https://doi.org/10.2355/isijinternational.41.590.

[65] D. Ahn, P. Sofronis, R. Dodds Jr., On hydrogen-induced plastic flow localization during void growth and coalescence, Int. J. Hydrogen Energy 32 (2007) 3734–3742, https://doi.org/10.1016/j.ijhydene.2006.08.047.

[66] A. Shibata, H. Takahashi, N. Tsuji, Microstructural and crystallographic features of hydrogen-related crack propagation in low carbon martensitic steel, ISIJ Int. 52 (2012) 208–212, https://doi.org/10.2355/isijinternational.52.208.

[67] M. Koyama, C.C. Tasan, E. Akiyama, K. Tsuzaki, D. Raabe, Hydrogen-assisted decohesion and localized plasticity in dual-phase steel, Acta Mater. 70 (2014) 174–187, https://doi.org/10.1016/j.actamat.2014.01.048.

[68] H. Matsunaga, H. Noda, Visualization of hydrogen diffusion in a hydrogen-enhanced fatigue crack growth in type 304 stainless steel, Metall. Mater. Trans. 42 (2011) 2696–2705, https://doi.org/10.1007/s11661-011-0661-8.

[69] W.W. Gerberich, Y.T. Chen, C.S. John, A short-time diffusion correlation for hydrogen-induced crack growth kinetics, Metall. Trans. 6 (1975) 1485–1498, https://doi.org/10.1007/BF02641960.

[70] P. Sofronis, R.M. McMeeking, Numerical analysis of hydrogen transport near a blunting crack tip, J. Mech. Phys. Solid. 37 (1989) 317–350, https://doi.org/10.1016/0022-5096(89)90002-1.

[71] A.T. Yokobori, T. Nemoto, K. Satoh, T. Yamada, Numerical analysis on hydrogen diffusion and concentration in solid with emission around the crack tip, Eng. Fract. Mech. 55 (1996) 47–60, https://doi.org/10.1016/0013-7944(96)00002-1.

[72] L. Qiao, W. Chu, X. Mao, Critical hydrogen concentration for hydrogen-induced cracking of type 321 stainless steel, Corrosion 52 (1996) 275–279, https://doi.org/10.5006/1.3293639.

[73] M. Wang, E. Akiyama, K. Tsuzaki, Determination of the critical hydrogen concentration for delayed fracture of high strength steel by constant load test and numerical calculation, Corrosion Sci. 48 (2006) 2189–2202, https://doi.org/10.1016/j.corsci.2005.07.010.

[74] J. Crank, The Mathematics of Diffusion, second ed., Oxford University Press, London, 1975.

[75] P. Tsong-Pyng, C.J. Altstetter, Effects of deformation on hydrogen permeation in austenitic stainless steels, Acta Metall. 34 (1986) 1771–1781, https://doi.org/10.1016/0001-6160(86)90123-9.

[76] J. Tien, A.W. Thompson, I.M. Bernstein, R.J. Richards, Hydrogen transport by dislocations, Metall. Trans. 7 (1976) 821–829, https://doi.org/10.1007/BF02644079.

[77] M. Dadfarnia, M.L. Martin, A. Nagao, P. Sofronis, I.M. Robertson, Modeling hydrogen transport by dislocations, J. Mech. Phys. Solid. 78 (2015) 511–525, https://doi.org/10.1016/j.jmps.2015.03.002.

[78] M. Shamsujjoha, S.R. Agnew, J.M. Fitz-Gerald, W.R. Moore, T.A. Newman, High strength and ductility of additively manufactured 316L stainless steel explained, Metall. Mater. Trans. 49 (2018) 3011–3027, https://doi.org/10.1007/s11661-018-4607-2.

[79] R.E. Reed-Hill, R. Abbaschian, Physical Metallurgy Principles, third ed., PWS Publishing, Boston (MA), 1994.